Article
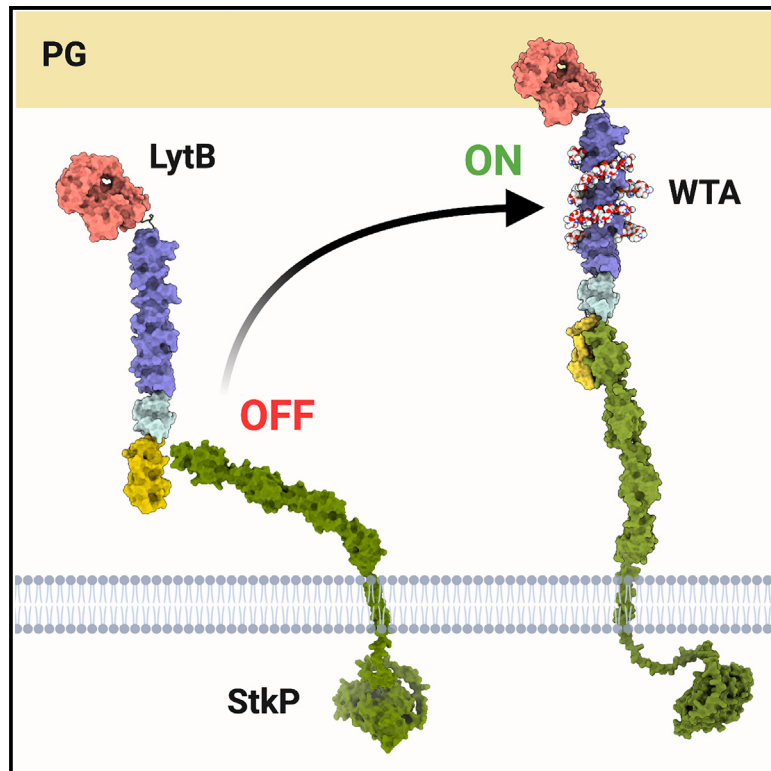
Molecular basis of the final step of cell division in *Streptococcus pneumoniae*

Graphical abstract

Authors

Siseth Martínez-Caballero, Céline Freton, Rafael Molina, ..., Shahriar Mobashery, Juan A. Hermoso, Christophe Grangeasse

Correspondence

xjuan@iqfr.csic.es (J.A.H.),
christophe.grangeasse@ibcp.fr (C.G.)

In brief

Martínez-Caballero et al. unveil the molecular mechanism of the final cell division step in *Streptococcus pneumoniae.* The combination of *in vivo*, *in vitro*, and *in silico* studies allows them to dissect the molecular dialogue between the cell-wall hydrolase LytB, wall teichoic acids, and the eukaryotic-like protein-kinase StkP.

Highlights

- Structures of the LytB$_{cat}$ domain disclose PG recognition and processing mechanisms

- LytB shows NM subdomains interacting with StkP and a C subdomain for WTA binding

- Characterization of full-length LytB highlights its dynamic modular organization

- The LytB/StkP/WTA interplay governs the final cell division step in streptococci

CellPress

Cell Reports

Article

Molecular basis of the final step of cell division in *Streptococcus pneumoniae*

Siseth Martínez-Caballero,[1,7,8] Céline Freton,[2,7] Rafael Molina,[1,7] Sergio G. Bartual,[1] Virginie Gueguen-Chaignon,[3] Chryslène Mercy,[2] Federico Gago,[4] Kiran V. Mahasenan,[5] Inés G. Muñoz,[6] Mijoon Lee,[5] Dusan Hesek,[5] Shahriar Mobashery,[5] Juan A. Hermoso,[1,*] and Christophe Grangeasse[2,9,*]

[1]Department of Crystallography and Structural Biology, Instituto de Química-Física "Rocasolano," Consejo Superior de Investigaciones Científicas, Madrid, Spain
[2]Molecular Microbiology and Structural Biochemistry, UMR 5086, Université de Lyon, CNRS, Lyon, France
[3]SFR Biosciences, Université de Lyon, CNRS UAR3444, ENS de Lyon, INSERM US8, Lyon, France
[4]Department of Biomedical Sciences & Instituto de Química Médica-CSIC Associated Unit, School of Medicine and Health Sciences, University of Alcalá, 28805 Alcalá de Henares, Spain
[5]Department of Chemistry and Biochemistry, University of Notre Dame, Notre Dame, IN 46556, USA
[6]Structural Biology Program, Spanish National Cancer Research Center (CNIO), 28029 Madrid, Spain
[7]These authors contributed equally
[8]Present address: Instituto de Química, Universidad Nacional Autonóma de México, Ciudad Universitaria, Ciudad de México 04510, Mexico
[9]Lead contact
*Correspondence: xjuan@iqfr.csic.es (J.A.H.), christophe.grangeasse@ibcp.fr (C.G.)
https://doi.org/10.1016/j.celrep.2023.112756

SUMMARY

Bacterial cell-wall hydrolases must be tightly regulated during bacterial cell division to prevent aberrant cell lysis and to allow final separation of viable daughter cells. In a multidisciplinary work, we disclose the molecular dialogue between the cell-wall hydrolase LytB, wall teichoic acids, and the eukaryotic-like protein kinase StkP in *Streptococcus pneumoniae*. After characterizing the peptidoglycan recognition mode by the catalytic domain of LytB, we further demonstrate that LytB possesses a modular organization allowing the specific binding to wall teichoic acids and to the protein kinase StkP. Structural and cellular studies notably reveal that the temporal and spatial localization of LytB is governed by the interaction between specific modules of LytB and the final PASTA domain of StkP. Our data collectively provide a comprehensive understanding of how LytB performs final separation of daughter cells and highlights the regulatory role of eukaryotic-like kinases on lytic machineries in the last step of cell division in streptococci.

INTRODUCTION

The bacterial cell wall provides shape and physical integrity against environmental stress. A cross-linked polymer, the peptidoglycan (PG), serves as the structural template for the cell wall. The PG is formed by glycan strands of varying lengths, comprising repeating disaccharide *N*-acetylglucosamine (NAG)-*N*-acetylmuramic acid (NAM). The NAM unit has a short peptide stem, where the cross-linking occurs between two neighboring glycan strands.[1] The PG and its biosynthesis pathway are targets of antibiotics, because of their critical role in bacterial survival.[2] Two types of PG synthases, the "shape, elongation, division, and sporulation" (SEDS) proteins and the "penicillin-binding proteins" (PBPs), are central to these processes.[3] Another series of enzymes, including PG hydrolases, are also involved in PG maturation and homeostasis. However, the full scope of these processes, and notably, the regulation of hydrolases, remains largely unknown.

Streptococcus pneumoniae (the pneumococcus) is an important human pathogen, which has served as a versatile model for the study of cytokinesis and morphogenesis.[4] In contrast to the established models such as *Bacillus subtilis* and *Escherichia coli*, where the nascent PG gets inserted at different cellular locations, the pneumococcus produces PG only at mid-cell.[5] The insertion of the nascent PG into the pneumococcus consequently serves the dual functions of synthesis for the elongation of the cell and for the formation of the septum.[6] It is understood that a tight synchronization of interplay among a set of PG hydrolases and synthases drives the process for the formation of the ovoid shape of the pneumococcal daughter cells. These events come about through the functions of PG synthases (two SEDS proteins and six PBPs) and the 13 PG hydrolases of pneumococcus, of which nine are known to participate in cell elongation and division.[7] Among these, the *N*-acetylglucosaminidase LytB, which cleaves the NAG-β(1,4)-NAM glycosidic bond of the PG backbone, is the only PG glycosyl hydrolase dedicated to the very late step of the cell-division process. In the absence of LytB, the pneumococcus forms long chains of daughter cells linked by the tip of the new cell pole.[8] LytB possesses a catalytic module positioned at the C-terminal end of an atypical modular structure composed of 18 sequential arrangements of choline-binding repeats (CBRs). This modular structure forms a
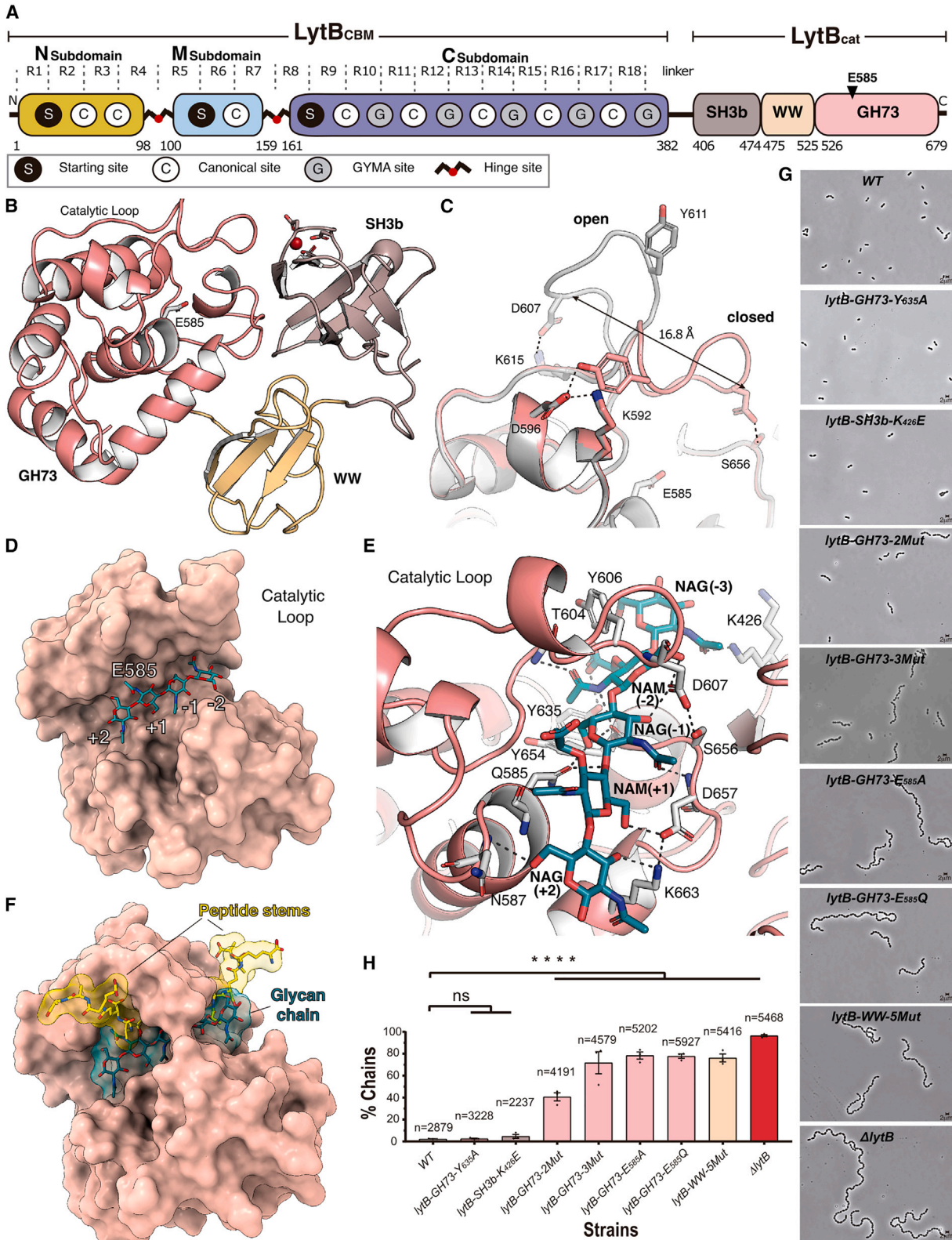
(legend on next page)

remarkably long choline-binding module (CBM), indeed the largest known within the choline-binding protein (CBP) family, which would allow LytB to anchor to the choline moieties of the teichoic acids (TAs) bound to the PG (known as wall teichoic acids; WTAs) or to membrane glycolipids (lipoteichoic acid; LTA).[9] Recently, it was demonstrated that the membrane serine/threonine kinase StkP, the central regulator of pneumococcal cell division, is key in positioning LytB at mid-cell within the PG layer.[10] More precisely, the extracellular domain of StkP interacts with LytB to drive its activity at mid-cell, which defines the thickness of the septal PG and final cell separation. These findings suggest that a molecular dialogue between LytB, the extracellular domain of StkP, and the choline-bound TAs is at play for LytB function on its specific substrate at the appropriate stage of cell division.

We report herein an integrative analysis that provides a comprehensive understanding of the mode of action of LytB and the means by which StkP directs its function. The crystallographic structures of the catalytic module of LytB in complex with synthetic substrates, supported by pneumococcal cell imaging, reveal the catalytic mechanism of LytB. The same methodological approach was used to pinpoint the role of the large CBM of LytB, highlighting the presence of three different subdomains. While one of them is able to specifically bind WTA, but not LTA, the two others are required for its localization at the division septum through interaction with StkP. Collectively, the work discloses the final step of cell separation during pneumococcal cytokinesis at atomistic resolution and provides an example of regulation by a eukaryotic-like kinase on bacterial lytic machineries.

RESULTS

The catalytic module of LytB presents two inactive/closed and active/open conformations

Sequence analysis reveals that LytB is composed of two main regions corresponding to the CBM (LytB$_{CBM}$, residues 1–381) and the catalytic module (LytB$_{cat}$, residues 406–679). The latter is further subdivided into the three domains SH3b, WW, and GH73[11] (Figure 1A). We solved the structure of LytB$_{cat}$ and found a similar arrangement for SH3b, WW, and GH73 domains as reported earlier, with root-mean-square deviation (RMSD) of 0.73 Å for the superimposition of 243 Cα atoms[11] (Figures 1B and S1). Importantly, we obtained the conformational details of the catalytic loop, which was missing in the earlier report. Indeed, this mobile loop presents two conformations, a closed and an open state, captured by two different structures at 1.78 and 1.43 Å resolution, respectively (Figures 1C and S1A–S1C). In the closed conformation, entrance to the active site is blocked, whereas in the open conformation the catalytic loop is sequestered ~17 Å away, exposing the large substrate-binding cavity (Figures 1C and S1B). Due to the high-quality electron-density maps, we were able to unambiguously trace the catalytic loop in its open and closed states (Figures 1B, 1C, and S1C) and to dissect the different interaction patterns in both conformations (Figure 1C). The conserved D607 residue stands out, as it establishes a salt bridge interaction with K615 in the open conformation, whereas in the closed conformation it is hydrogen bonded to S656 (Figure 1C). As detailed below, residue D607 together with other amino acids of the loop play a relevant role in substrate stabilization and hydrolysis.

LytB substrate recognition and catalytic activity depend on the catalytic loop

We co-crystallized LytB$_{cat}$ with the substrate analog NAG-NAG-NAG-NAG (NAG$_4$) (Figure S2A), lacking the NAM moieties, but which can be degraded by LytB at a very low rate. The structure of the LytB$_{cat}$:NAG$_4$ complex was solved at 1.55 Å resolution (Figure 1D and Table S1). The substrate-binding cleft of lysozymes and other glycosyl hydrolases accommodates several saccharide units at subsites designated as positions −i (the non-reducing end) through +j (in the other direction). The saccharide units flanking the scissile glycosidic bond are designated as positions −1 and +1. The structure of the LytB$_{cat}$:NAG$_4$ complex showed an open conformation for the catalytic loop, with the tetrasaccharide occupying subsites −2, −1, +1, and +2 (Figures S2B and S2C). The interaction pattern observed in the catalytic loop for the apo open conformation is lost in this NAG$_4$-bound state, indicating that NAG$_4$ promotes changes in

---

Figure 1. Substrate recognition by the catalytic module of LytB

(A) Schematic representation of the modular nature of LytB is shown. The 18 repeats (R1–R18) composing the choline-binding module of LytB are labeled. The position of the catalytic residue E585 is indicated by a triangle.

(B) Apo structure of the complete catalytic module of LytB in its closed conformation. The three domains building the catalytic module are colored differently and labeled. The catalytic E585 residue is represented as capped sticks and labeled. The calcium ion found attached to the SH3b domain is represented as a red sphere and coordinating residues as capped sticks.

(C) Detailed view of the differences in the catalytic loop between the closed (salmon) and the open (gray) conformations in the apo state. Some relevant residues are represented as capped sticks and labeled. Polar contacts are represented as dotted lines.

(D) Three-dimensional structure of the LytB$_{cat}$:NAG$_4$ complex in its open conformation, with NAG$_4$ depicted in capped sticks colored by atom type (green for the carbons). Sites occupied by the ligand are labeled.

(E) Detailed view of substrate recognition by LytB as observed in the LytB$_{cat-E585Q}$:(NAG-NAM)$_2$ complex. Substrate spanning from site −3 to +2 is depicted as capped sticks colored by atom type (green for carbon). Relevant active-site residues are given in capped sticks (colored white for carbons) and labeled. Hydrogen-bond interactions are represented as dotted lines.

(F) LytB$_{cat}$:PG fragment complex model in its closed conformation. Peptide stems and glycan chains are colored by atom type with yellow and dark green for carbon atoms, respectively.

(G) Phase-contrast microscopy images of WT, lytB-GH73-Y$_{635}$A, lytB-SH3b-K$_{426}$E, lytB-GH73-2Mut (Y$_{606}$A/D$_{607}$K), lytB-GH73-3Mut (Y$_{654}$A/S$_{656}$A/D$_{657}$K), lytB-GH73-E$_{585}$A, lytB-GH73-E$_{585}$Q, lytB-WW-5Mut (Y$_{477}$A/E$_{479}$K/Y$_{486}$A/Y$_{488}$A/Y$_{511}$A), and ΔlytB cells. Scale bar, 2 μm.

(H) Percentage of cells with a chaining phenotype (minimum four cells per chain), and n indicates the number of cells scored from three independent experiments. The error bar and the data points overlapping the histogram (mean of three experiments) represent the SEM and the mean of each experiment, respectively. Statistical comparison was done with one-way ANOVA with Tukey's multiple comparison test. ****$p < 0.0001$ and ns, not significant, $p > 0.05$.
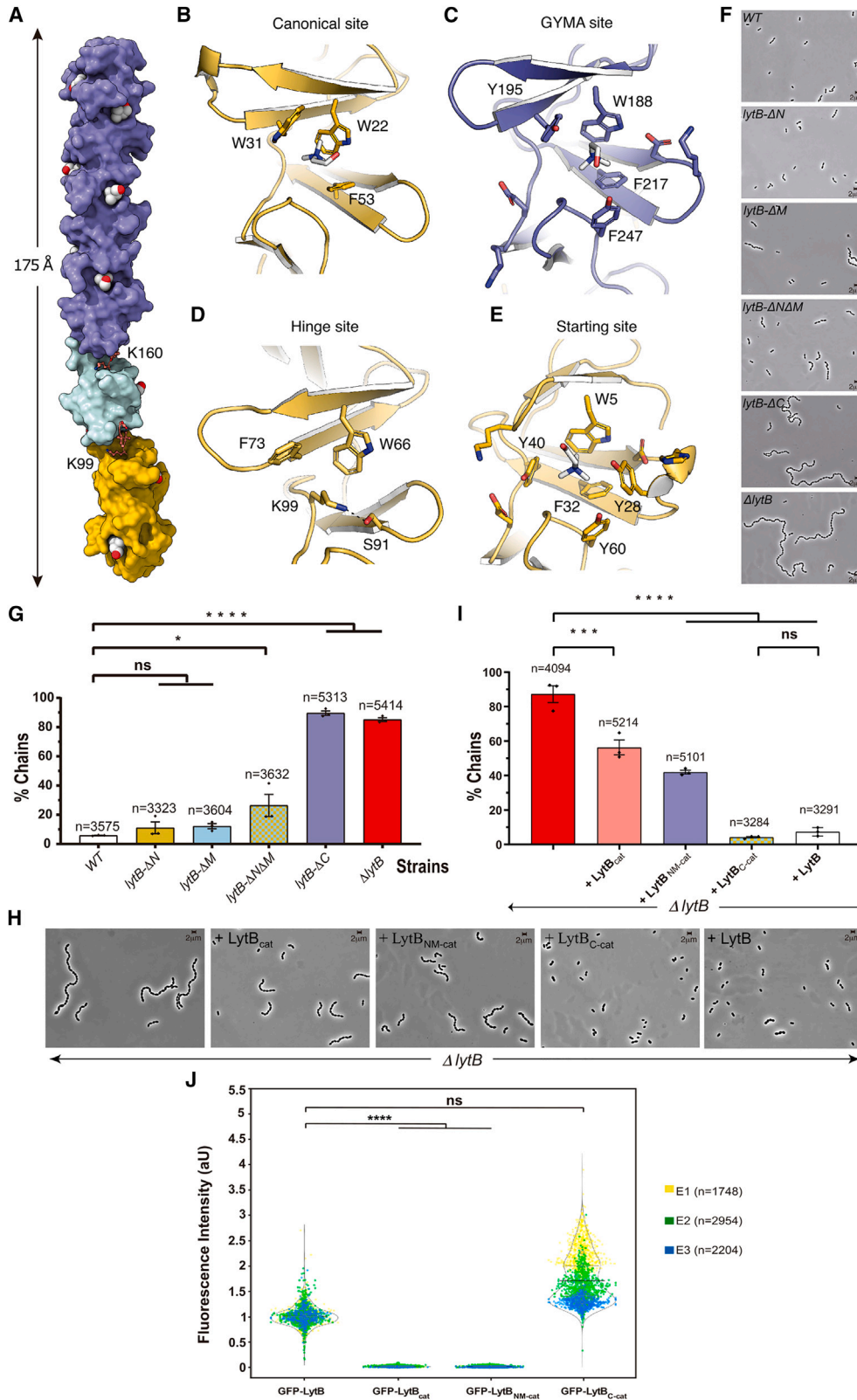
the organization of the catalytic loop. Notably, D607 interacts with K615 in the apo form, whereas it interacts with T609 in the $LytB_{cat}$:NAG_4 complex (Figure S2B). These two conformations suggest the route to the closed conformation. To explore PG recognition by LytB, we solved the structures of the catalytically inactive variant $LytB_{cat-E585Q}$ alone and in complex with the substrate NAG-NAM-NAG-NAM-OCH$_3$ (Figure S2A) (herein referred to as tetrasaccharide $(NAG-NAM)_2$) (Table S1). This structure, mimicking the polymeric natural substrate, was synthesized for this study, and it corresponds to the native PG strand devoid of the stem peptide. As expected, the apo $LytB_{cat-E585Q}$ variant shows a conformational state that is identical to that of wild-type $LytB_{cat}$ (RMSD of 0.08 Å for 264 Cα atoms superimposition) (Figure S2D). Two different structures for the $LytB_{cat-E585Q}$:$(NAG-NAM)_2$ complex were solved at 1.5 Å (Figure S2F) and 1.3 Å resolution (Figure S2G). Both structures showed the closed conformation for the $LytB_{cat}$ with the catalytic loop capping the active-site-bound substrate. Interestingly, the tetrasaccharide occupies subsites −3, −2, −1, and +1 in one of them (Figure S2F), whereas it is distributed in two populations, spanning the subsites −3 to +2 in the second structure that overlap at sites −1 and +1 (the cleavage site) (Figure S2G). In both cases, the overlapping sugar rings adopt strictly the same conformation (Figure S2E) and give rise to an identical number of interactions with the protein (Figure S2H). However, the $LytB_{cat-E585Q}$:$(NAG-NAM)_2$ showing two partially overlapping $(NAG-NAM)_2$ molecules reveals information about an extra site (−3 position) in the LytB active site. These complexes allowed us to map all the amino acids involved in stabilization of the glycan chain (Figure 1E). Interestingly, direct modeling of peptide stems onto the $LytB_{cat-E585Q}$:$(NAG-NAM)_2$ complex reveals that there is no steric impediment for the peptide stems (Figure 1F), but accommodation of cross-linked PG is unlikely. Overall, our structures depicted a model of PG recognition by LytB (Figure S2I).

To assess the physiological relevance of our findings in live bacteria, we generated mutations of some of the amino acids involved in the interactions with $(NAG-NAM)_2$ in the chromo-somal copy of *lytB* and analyzed their impact on cell separation (Figures 1G and 1H). As control, and as already described, the main phenotype resulting from the deletion of *lytB* was the presence of cell chaining.[10] Here, we calculated that only 3% of wild-type (WT) cells formed chains, whereas 95% of Δ*lytB* cells did so (Figures 1G and 1H). In agreement with our structural analysis, single replacement of the catalytic glutamate, by glutamine or alanine (strains *lytB-GH73-E$_{585}$Q* and *lytB-GH73-E$_{585}$A*), is sufficient to result in cell chaining equivalent to that observed in Δ*lytB* cells (Figures 1G and 1H). Likewise, amino acid substitutions of active-site residues Y654, S656, D657 (strain *lytB-GH73-3Mut*; Figure 1E), and part of the YAT/SD motif, a signature of the GH73 family,[12] also resulted in strong cell chaining (Figures 1G and 1H). Importantly, the cell chaining observed for the Y606A-D607K variant (strain *lytB-GH73-2Mut*) (Figures 1G and 1H), while not critical like the E585, reveals an important effect *in vivo* supporting the relevance of these residues in substrate recognition and confirming the role of the catalytic loop in the enzymatic activity of LytB (Figures 1D, 1F, and S2H). It is worth mentioning that replacement of the four Tyr residues and one Glu in the exposed Tyr-rich patch of the WW domain (strain *lytB-WW-5Mut*) also led to strong cell chaining (Figure 1G).
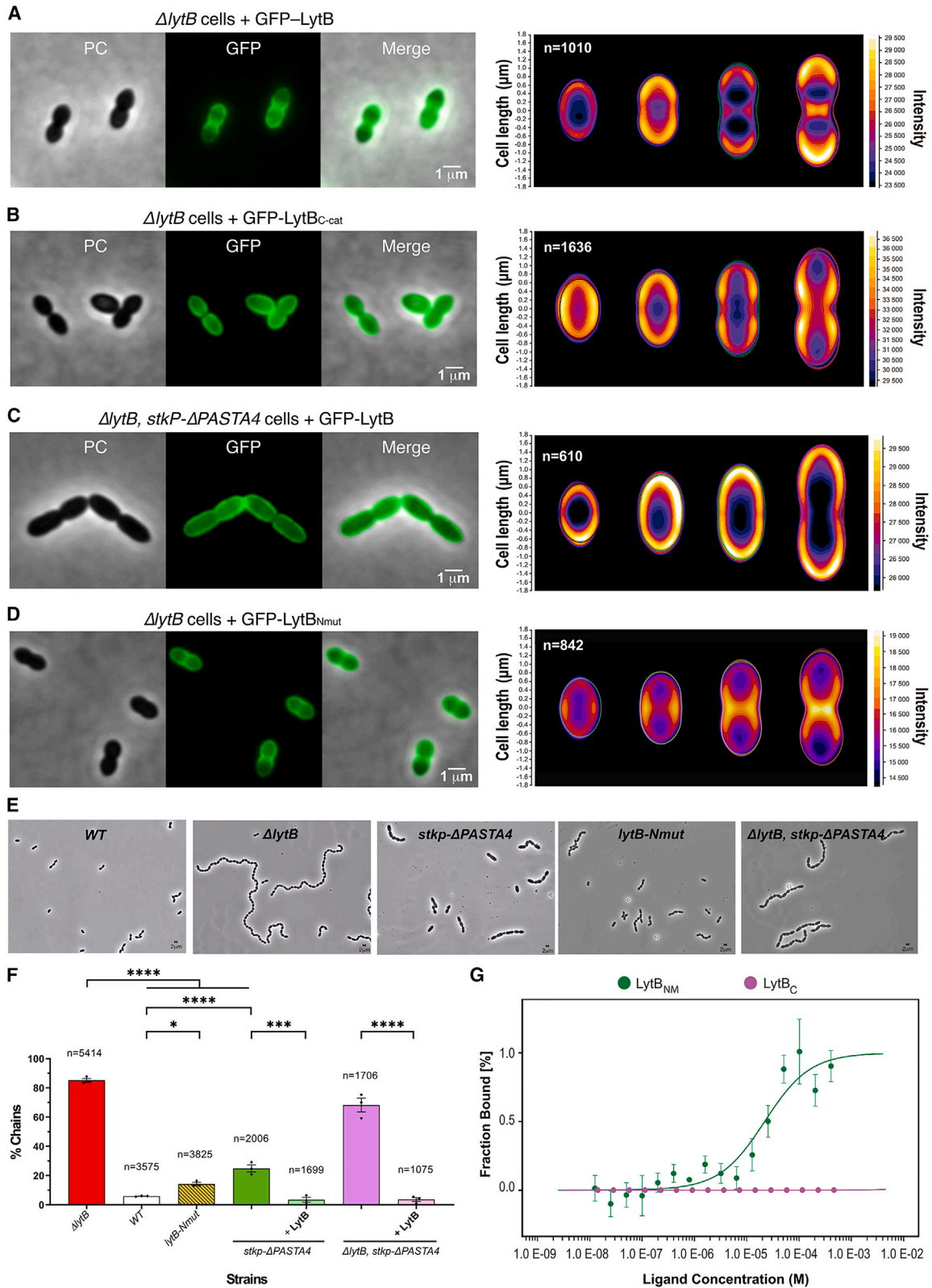
In summary, our findings show that the catalytic module presents different states (open, intermediate, closed) controlled by the catalytic loop. The binding site accommodates PG chains (with or without peptide stems) of at least five sugars. The WW domain, unique among the GH73 family members, is also important for substrate binding *in vivo*.

The CBM of LytB is segregated in three distinct subdomains

CBMs are responsible for cell-wall anchorage through recognition of TA. As the CBM of LytB ($LytB_{CBM}$) is unusually long (18 CBRs, annotated R1 to R18, forming nine potential choline-binding sites [CBSs]; Figure 1A), we solved the three-dimensional structure of the full-length $LytB_{CBM}$ in complex with choline (Figure 2A and Table S2).

Figure 2. Structure and role of the choline-binding module of LytB

(A) The molecular surface representation of the complete $LytB_{CBM}$ with each subdomain colored differently is given: N subdomain is colored in yellow, M subdomain is colored in cyan, and C subdomain is in blue. Choline molecules bound to $LytB_{CBM}$ are represented as spheres. The hinge regions (located around K99 and K160 residues) are depicted in orange cartoon with side chains in ball-and-stick representation. Lys residues at the hinge regions are labeled.

(B) Three-dimensional structure of a canonical choline-binding site (C2) in LytB.

(C) Structure of a GYMA choline-binding site (GYMA 2) in LytB.

(D) Structure of a hinge site (hinge 2) in LytB.

(E) Structure of a starting choline-binding site (S1) in LytB. Aromatic residues involved in the cation-π interactions with choline and other relevant residues are represented as capped sticks and labeled. Choline molecule are shown as spheres colored by atom type with carbons in white.

(F) Phase-contrast microscopy images of WT, *lytB-ΔN*, *lytB-ΔM*, *lytB-ΔNΔM*, *lytB-ΔC*, and Δ*lytB* cells; scale bar, 2 μm.

(G) Percentage of cells with a chaining phenotype (minimum four cells per chain), with n indicating the number of cells scored from three independent experiments. The error bar and the data points overlapping the histogram (mean of three experiments) represent the SEM and the mean of each experiment, respectively. Statistical comparison was done with one-way ANOVA with Tukey's multiple comparison test. ****p < 0.0001, *p < 0.05, and ns, not significant, p – 0.05.

(H–J) Impact of exogenously added LytB or derivatives on Δ*lytB* cell chaining. (H) Δ*lytB* cells were treated with LytB or $LytB_{cat}$ or $LytB_{NM-cat}$ or $LytB_{C-cat}$ and then imaged. Phase-contrast images. Scale bar, 2 μm. (I) Percentage of cells with a chaining phenotype (minimum four cells per chain). n indicates the number of cells scored from three independent experiments. The error bar and the data points overlapping the histogram (mean of three experiments) represent the SEM and the mean of each experiment, respectively. Statistical comparison was done with one-way ANOVA with Tukey's multiple comparison test. ****p < 0.0001, ***p < 0.001, and ns, not significant, p > 0.05. (J) Total fluorescence of GFP-LytB, GFP-$LytB_{cat}$, GFP-$LytB_{NM-cat}$, and GFP-$LytB_{C-cat}$ bound to Δ*lytB* cells. A super-violin plot with data from three independent experiments in yellow, green, and blue is shown. The error bar, the data points, and the black horizontal line represent the SEM, the median of each experiment, and the mean of the three experiments, respectively. Data obtained with GFP-$LytB_{cat}$, GFP-$LytB_{NM-cat}$, and GFP-$LytB_{C-cat}$ were normalized to data with GFP-LytB taken as 1. Statistical comparison was done using t test. ****p < 0.0001 and ns, not significant.

A *ΔlytB* cells + GFP–LytB

B *ΔlytB* cells + GFP-LytB$_{C-cat}$

C *ΔlytB, stkP-ΔPASTA4* cells + GFP-LytB

D *ΔlytB* cells + GFP-LytB$_{Nmut}$

E WT ΔlytB stkp-ΔPASTA4 lytB-Nmut ΔlytB, stkp-ΔPASTA4

F %Chains vs Strains

G LytB$_{NM}$ LytB$_C$ — Fraction Bound [%] vs Ligand Concentration (M)

(legend on next page)

Some CBSs of LytB$_{CBM}$ follow the well-defined architecture, denoted C for canonical in Figures 1A and 2B and previously identified in all the other CBPs,[9] in which the choline molecules are stabilized by cation-π interactions with three structurally conserved aromatic residues from two adjacent CBRs. Unexpectedly, three additional types of CBSs were also found in LytB$_{CBM}$ (Figures 1A and 2B–2E). The first non-canonical CBS type includes the GYMA site (named G) (Figure 2C), which comprises the Gly-Tyr-Met-Ala (GYMA) motif first described in the cell-wall hydrolase LytC.[13] However, LytB GYMA sites are composed of four aromatic residues (Figure 2C) instead of the six aromatic residues previously observed in LytC.[13] The other two non-canonical CBS types, herein named H and S, have never been described before. The type H (for hinge) is found twice in the LytB$_{CBM}$, between R4 and R5 and between R7 and R8, and has lost the ability to bind choline (Figure 2D). Indeed, the H-type CBS lacks enough aromatic residues to stabilize the choline moiety, and the side chains of residues K99 and K160 occupy the space where choline is normally lodged in the canonical CBS (Figures 1A and 2D). The other non-canonical CBS (denoted S for "starting" in Figures 1A and 2E) is composed of five aromatic residues and placed at the beginning of each of the three domains identified in LytB$_{CBM}$ (see below).

The distribution of the four CBS types (canonical, GYMA, hinge, and starting) defines three structurally independent subdomains in the LytB$_{CBM}$, named N (for N terminus), M (for middle), and C (for C terminus) (Figure 1A). Indeed, the two H-type CBSs act as hinge regions connecting the three N, M, and C subdomains (Figures 1A and 2A). Each subdomain starts with an S-type CBS and presents a unique combination of CBSs. While the N and M subdomains contain only canonical sites, the C subdomain includes G-type sites alternating with C-type sites (Figure 1A).

To validate the role of hinges in dividing the full-length LytB$_{CBM}$ into three subdomains, we also solved the structure of the LytB region encompassing R1 to R8 (LytB$_{NM}$, residues 1–185) at 2.0 Å resolution (Table S2). Importantly, structural superimposition of this construct onto the full-length LytB$_{CBM}$ revealed important conformational differences (RMSD of 1.68 Å for the superimposition of 182 Cα atoms). The structural analysis showed that, while the three-dimensional structures of N and M subdomains are preserved in both constructs (RMSD of 0.44 Å for N subdomain superimposition and 0.43 Å for M subdomain superimposition), an important rearrangement of the N and M subdomains occurs around the hinge site. Considering these motions and the length of LytB$_{CBM}$, the two identified hinge regions appear to provide great flexibility to LytB$_{CBM}$ and internal mobility among its three distinct subdomains, as further confirmed by both molecular dynamics (MD) simulations and small-angle X-ray scattering (SAXS) experiments in solution (*vide infra*).

The C subdomain is essential for LytB activity

To determine the respective, and potentially different, functions of the three domains of the LytB$_{CBM}$, we constructed a series of pneumococcal mutants in which the chromosomal copy of *lytB* is deprived of one of the three N, M, or C subdomains. Deletion of either the N (strain *lytB-ΔN*) or the M (strain *lytB-ΔM*) subdomain induced a weak and non-statistically relevant increase in cell chaining (Figures 2F and 2G), which was, however, cumulative and reproducible (mean value 26.4%) upon deletion of both subdomains (strain *lytB-ΔNΔM*). In contrast, deletion of the C subdomain (strain *lytB-ΔC*) had a drastic effect leading to a degree of cell chaining similar to that of Δ*lytB* cells (Figures 2F and 2G). These observations show that the C subdomain is crucial for the function of LytB. To confirm the validity of this statement, we purified the LytB protein variants that are devoid of different parts of the CBM and added them exogenously to Δ*lytB* cells to determine their ability to reverse cell chaining (Figures 2H and 2I). As a control, addition of the WT LytB resulted in almost total depletion of cell chaining (mean value 7.3% of chained cells). When cells were incubated with the catalytic domain LytB$_{cat}$ or LytB devoid of the C subdomain (LytB$_{NM-cat}$; form equivalent to that produced by the strain *lytB-ΔC*), a large number of cells remained chained (mean value 56.3% and 42%, respectively). By contrast, a complete loss of chaining was detected upon incubation with LytB$_{C-cat}$ that was equivalent to the form produced by the strain *lytB-ΔNΔM* (Figures 2H and 2I). Taken together, these observations show that LytB requires the C subdomain to be fully active when added exogenously.

The low number of CBSs present in the N and M subdomains (with three and two CBSs, respectively) contrasts with the 11 sites found at the C subdomain. To assess whether this difference can account for the higher capacity of the C subdomain to promote LytB-mediated cell-chain separation, we analyzed the binding and the cellular localization of LytB constructs fused to green fluorescent protein (GFP). As previously reported, purified and exogenously added GFP-LytB efficiently binds pneumococcal cells and localizes at the division septa and at the cell poles[14] (Figures 2J and 3A). We note that both GFP-LytB$_{cat}$ and GFP-LytB$_{NM-cat}$ cannot efficiently bind to the cell surface (Figure 2J). On the other hand, GFP-LytB$_{C-cat}$ bound

Figure 3. Interplay between the LytB NM domain and the StkP-PASTA4 repeat

(A and B) Δ*lytB* cells were treated with GFP–LytB (A) or GFP-LytB$_{C-Cat}$ (B) and then imaged. Phase contrast (PC, left), GFP fluorescent signal (middle), and overlays (right) are shown; scale bar, 1 μm. The corresponding heat maps representing the localization patterns of GFP-LytB and GFP-LytB$_{C-cat}$ are shown on the right. The n value represents the number of cells analyzed in a single representative experiment made in triplicate.

(C) Same as (A) and (B) with Δ*lytB-stkP-ΔPASTA4* cells treated with GFP-LytB.

(D) Same as (A) and (B) with Δ*lytB* cells treated with GFP-LytB$_{Nmut}$.

(E) Phase-contrast microscopy images of WT, *stkP-ΔPASTA4*, *lytB-Nmut*, Δ*lytB*, and Δ*lytB-stkP-ΔPASTA4* cells. Scale bar, 2 μm.

(F) Percentage of cells with a chaining phenotype (minimum four cells per chain) from three independent experiments. The error bar and the data points overlapping the histogram (mean of three experiments) represent the SEM and the mean of each experiment, respectively. Statistical comparison was done with one-way ANOVA with Tukey's multiple comparison test. ****p < 0.0001, ***p < 0.001, and *p < 0.05.

(G) Microscale thermophoresis binding assays of labeled LytB$_{NM}$ (green dots) or LytB$_{C}$ (purple dots) domains to increasing concentrations of the StkP-PASTA4 repeat. The fraction bound is plotted against the ligand concentration.. Measurements are represented by dots (mean of three independent experiments) and the fitted curve by a line. The error bar represents the standard deviation.
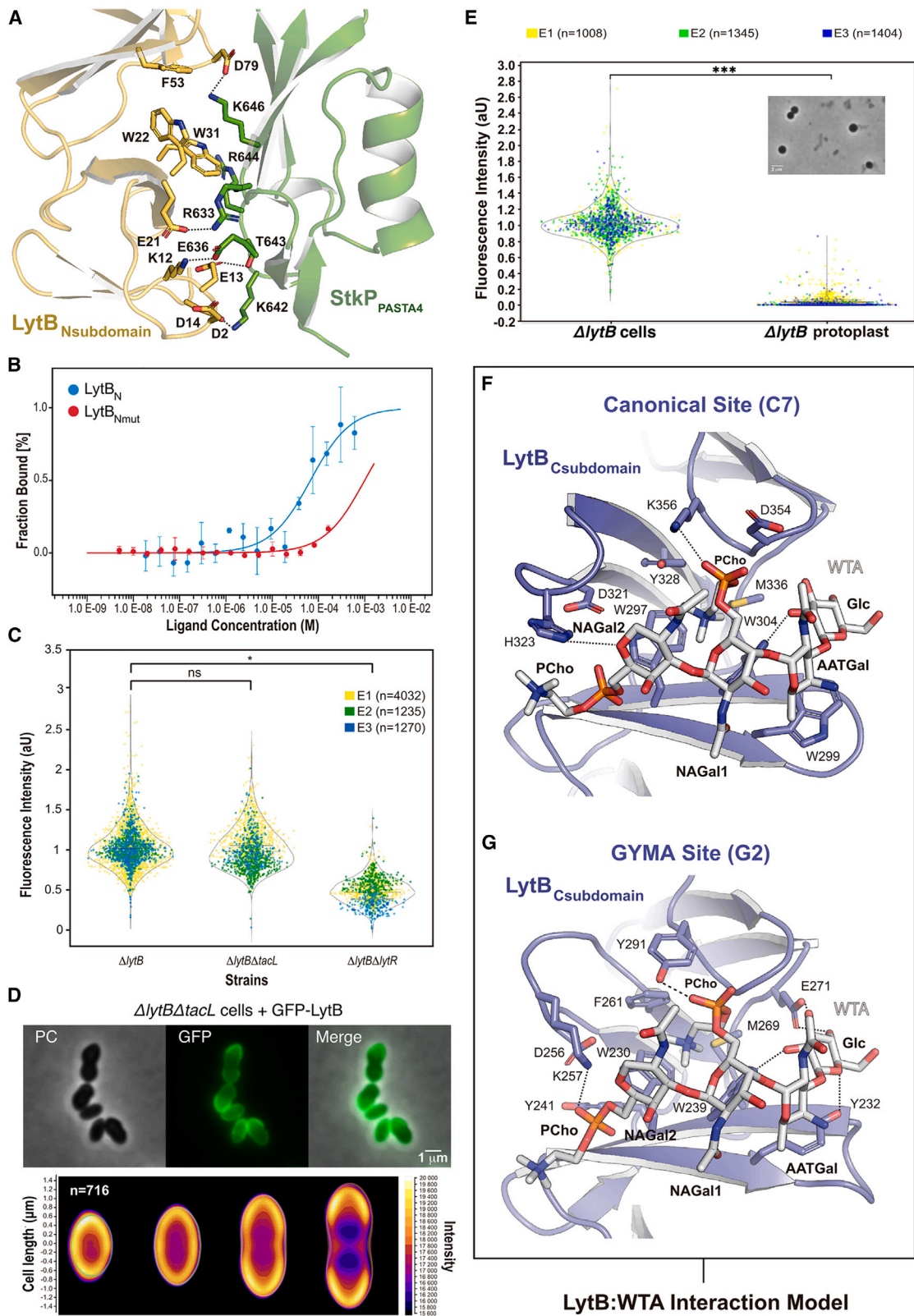
(legend on next page)

pneumococcal cells, like GFP-LytB did, but it displayed a different localization pattern with no labeling of the pole and the division septum (Figures 2J and 3B). These data confirm that the C subdomain is fundamental for the interaction of LytB with the cell wall, but not sufficient to drive the localization of LytB at the division septum.

The NM subdomains interact with the distal PASTA4 repeat of StkP

Recently, it was shown that deletion of the fourth and distal PASTA repeat (termed PASTA4) in StkP leads to cell chaining and aberrant localization of LytB to the periphery of the cells.[10] These two phenotypes are similar to those observed with the *lytB-ΔNΔM* mutant, even if there is a small difference in fluorescence repartition around the cell, probably due to the impaired division of the *ΔlytB-stkP-ΔPASTA4* (compare Figures 3B, 2F, and 2G with Figures 3C, 3E, and 3F, respectively). In addition, cell chaining of *ΔlytB-stkP-ΔPASTA4* and *stkP-ΔPASTA4* cells is abolished upon treatment with exogenous LytB (Figure 3F). We therefore hypothesized that the interplay between the N and M subdomains of LytB and StkP PASTA4 could be key in controlling LytB function and localization. To test this, we produced and purified the NM and C subdomains of LytB and checked their interaction with StkP PASTA4 by microscale thermophoresis (Figure 3G). The results show reproducible interactions between PASTA4 and the NM domain ($K_D = 22$ μM), while no interaction was detected between PASTA4 and the C subdomain (Figure 3G).

Interestingly, both structural analysis and protein-protein docking procedures revealed a potential binding site in the LytB-NM domain for StkP-PASTA4 (Figure 4A). The ensuing atomistic MD simulations revealed a very stable interaction over a 300-ns trajectory. Most noteworthy are the electrostatic interactions between charged residues in both proteins, but also through the insertion of K646 from StkP-PASTA4 into the canonical CBS of the LytB-N subdomain (Figures 4A and S3A). Importantly, the interacting residues of the StkP-PASTA4 (R633, E636, K642, R644, and K646) (Figures 4A and S3A)

were those previously identified as responsible for the StkP-LytB interaction (Figure S3B).[10] Our model also predicts that residues K12, E13, D14, and E21 from the LytB-N subdomain play a role in the interaction with StkP-PASTA4 (Figures 4A and S3B). To validate this model, we replaced these four residues with alanines and analyzed the complex formation both *in vitro* and *in vivo*. Microscale thermophoresis revealed that the interaction between StkP-PASTA4 and the LytB-N subdomain containing mutations K12, E13, D14, and E21 (domain Nmut) is abolished (Figure 4B). On the other hand, pneumococcal cells producing LytB variants at the same amino acids (*lytB-Nmut*) showed a mild cell-chaining pattern reminiscent of that of *lytB-ΔN* and *stkP-ΔPASTA4* cells (Figures 2F, 2G, 3E, and 3F). Last, localization of exogenously added GFP-LytB-Nmut is altered with no labeling of the poles and some fluorescence diffused in the membrane (compare Figure 2I with 3D). Altogether, these data show that LytB and StkP interact through their respective NM and PASTA4 regions and provide the molecular details of the interaction.

The C subdomain selectively binds wall teichoic acids rather than lipoteichoic acids

Our finding that LytB$_{C-cat}$ still allows cell separation and localizes on the entire cell surface (Figures 2F, 2G, and 3B) confirms that the C subdomain is sufficient to anchor exogenously added LytB to the cell wall through interaction with TAs. We then focused on determining whether the C subdomain would preferentially interact with either the WTAs or the LTAs. To this end, we generated two strains deficient in either *tacL* or *lytR*, which are proposed to link TA subunits only to the membrane acceptor (LTA) or to PG (WTA), respectively.[15,16] We then evaluated binding of GFP-LytB mutants to the cell surface of *ΔlytB*, *ΔlytBΔtacL*, or *ΔlytBΔlytR* cells. While GFP-LytB binding to *ΔlytBΔtacL* cells was as efficient as to *ΔlytB* cells, the fluorescence intensity displayed by *ΔlytBΔlytR* cells was drastically reduced (Figure 4C). When we performed the same experiment with GFP-LytB$_{C-cat}$, devoid of the N and M subdomains, a similar reduction of the labeling of *ΔlytBΔlytR* cells was observed (Figure S4A). Although

Figure 4. Teichoic acid and StkP recognition by LytB

(A) Zoom view of the interaction interface between StkP-PASTA4 (green) and subdomain N (dark yellow) of LytB, displaying its key interacting residues in sticks.

(B) Microscale thermophoresis binding assays of labeled LytB$_N$ (blue dots) or LytB$_{Nmut}$ (red dots) domains to increasing concentrations of the StkP-PASTA4 repeat. The fraction bound is plotted against the ligand concentration. Measurements are represented by dots and the fitted curve by a line. The error bar represents the standard deviation.

(C) Total fluorescence of GFP-LytB bound to *ΔlytB*, *ΔlytBΔtacL*, and *ΔlytBΔlytR* cells. A super-violin plot with data from three independent experiments in yellow, green, and blue is shown. The error bar, the data points, and the black horizontal line represent the SEM, the median of each experiment, and the mean of the three experiments, respectively. Data from *ΔlytBΔtacL* and *ΔlytBΔlytR* cells were normalized to *ΔlytB* data taken as 1. Statistical comparison was done using t test. *p < 0.05 and ns, not significant, p > 0.05.

(D) *ΔlytBΔtacL* cells were treated with GFP-LytB and then imaged. Phase contrast (PC, left), GFP fluorescent signal (middle), and overlays (right) are shown; scale bar, 1 μm. The corresponding heatmaps representing the localization patterns of GFP-LytB are shown on the bottom. The n value represents the number of cells analyzed in a single representative experiment made in triplicate.

(E) Total fluorescence of GFP-LytB bound to *ΔlytB* cells or protoplasts. A super-violin plot with data from three independent experiments in yellow, green, and blue is shown. The error bar, the data points, and the black horizontal line represent the SEM, the median of each experiment, and the mean of the three experiments, respectively. Data obtained with protoplasts were normalized to data with cells taken as 1. Statistical comparison was done using t test. ***p < 0.001. The phase-contrast image shows the pneumococcal protoplasts generated upon treatment with lysozyme and mutanolysin; scale bar, 2 μm.

(F) Zoom view of canonical choline-binding site C7 of the subdomain C (slate) represented in cartoon and displaying its key interactions with teichoic acids (carbons colored in white) depicted in sticks.

(G) Zoom view of GYMA choline-binding site G2 of the subdomain C (slate) represented in cartoon and displaying its key interactions with teichoic acids (carbons colored in white) depicted in sticks.
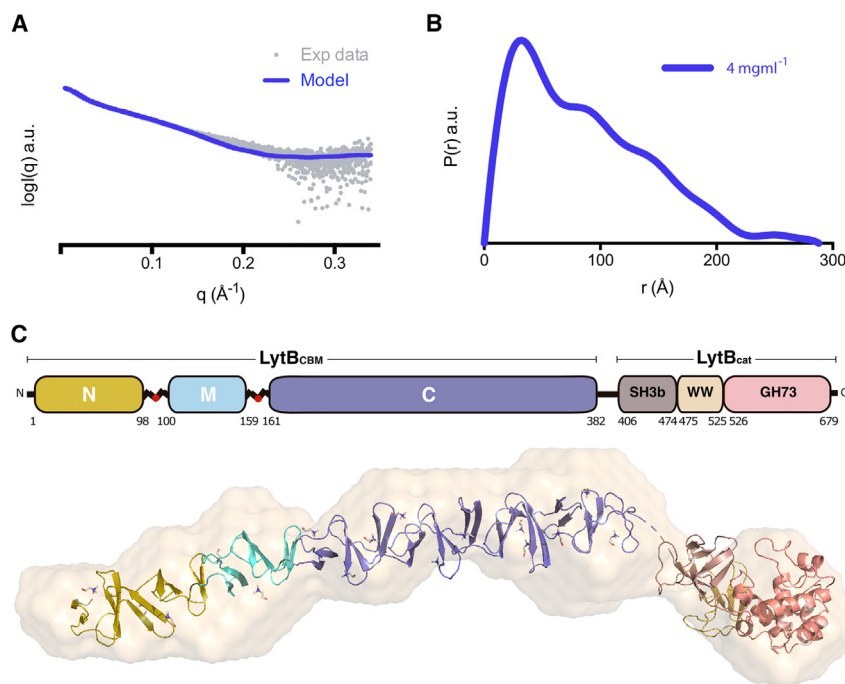
Figure 5. SAXS analysis of full-length LytB in solution

(A) Experimental scattering curve (dots) and theoretical scattering curve computed for the model of LytB (smooth) at 4 mg mL^{-1} concentration.

(B) The plot shows the normalized pair-distance distribution function P(r) for LytB (blue graph). a.u., arbitrary units.

(C) Overlaying of the *ab initio* determined SAXS envelope for LytB with the model based on the crystal structures reported here. The different regions of the generated model are displayed following the Figure 1A coloring code, and the envelope is colored in light orange.

tions showed a stable attachment of PCho molecules to LytB$_{CBM}$, but a fast detachment of PEA from LytB$_{CBM}$ under the same simulation conditions (Video S1).

Full-length LytB presents a high plasticity

All our attempts to obtain well-diffracting crystals with full-length LytB turned out to be unsuccessful, which suggested a dynamic nature of the protein. We investigated the dynamics of the full-length LytB in solution by SAXS experiments and by MD simulations. The SAXS results (Figure 5 and Table S3) revealed that the protein presents an extended structure in solution that agrees with the dimensions of the full-length structural model proposed from the sum of the separate crystal structures. In parallel, we performed four MD simulations of the full-length LytB, each with the catalytic module placed in a distinct orientation for the starting point of the simulation, as allowed by the flexible linker loop (Figure S5). The MD simulations over 400 ns each revealed a highly dynamic protein (Figure S5 and Video S2). The linker contributed to a pronounced motion of the catalytic module and allowed the catalytic site to reach a radius of >60 Å around the CBM, while the bending and swaying motion of the LytB$_{CBM}$ was further extended so as to reach the active site. In essence, the simulations sampled all four starting points for the catalytic module. The fact that we did not observe any particular preferred orientation of the catalytic module with respect to LytB$_{CBM}$ throughout the simulation time indicates that the enzyme is likely to function within a specific radius of its anchoring location in the cell wall.

DISCUSSION

The catalytic module of LytB presents unique features among the GH73 family members, including the presence of SH3b and WW domains. Our studies revealed that amino acids of the SH3b and WW domains directly contribute to substrate stabilization. These two additional domains thus make up a large, narrow, and deep groove, creating the catalytic site (Figure S6). This arrangement is complemented by the distinct catalytic loop conformations, which enable substrate sequestration and catalysis. In this process, the conserved D607 residue plays a crucial

the deletion of *tacL* generates cell morphology defects, we observed that the localization of GFP-LytB and GFP-LytB$_{C-cat}$ in Δ*lytB*Δ*tacL* cells is reminiscent of that in Δ*lytB* cells with polar or membrane labeling, respectively (Figures 4D and S4B). Moreover, protoplasts devoid of PG and WTA were not labeled by GFP-LytB (Figure 4E) Altogether, these data show that the C subdomain preferentially binds WTA but not LTA, whereas the N and M subdomains serve as the binding domains for the PASTA4 repeat of StkP.

WTA binds more strongly to G sites than to C sites

The LytB$_{CBM}$:choline complex was used as a template to model how WTAs are recognized by LytB and then subjected to MD simulations. The four cyclic sugars in the WTA repeating unit keep a compact conformation around the aromatic residues building the CBS during the simulated trajectories (Figures 4F and 4G), whereas the ribitol-phosphate moiety provides flexibility to WTA. Remarkably, while a similar arrangement is observed for the WTA bound to C-type or G-type CBS, our model shows that G sites stabilize sugar components of WTA, by both CH-π[17] and polar interactions, more strongly than C sites do (Figures 4F and 4G). Thus, LytB-C subdomain anchors to the pneumococcal cell wall through strong interactions with both the phosphorylcholine (PCho) linked to WTA (through cation-π interactions and hydrogen bonds to the phosphate, Figures 4F and 4G) and other components of the WTA unit through the G sites.

In the pioneering work by Alexander Tomasz[18] it was shown that replacement of choline moieties by ethanolamine resulted in loss of activity by pneumococcal autolysins and was associated with increases in cell chaining.[18] Our models of LytB in complex with either PCho or phosphorylethanolamine (PEA) provide a molecular rationale for this phenomenon, as the MD simula-

role by establishing polar interactions with both the S656 residue from the binding site and the substrate glycan chains (Figure 1E). Last, and importantly, our observations show that the active site of LytB can accommodate long glycan chains, regardless of the presence of the peptide stem (Figure 1F). However, our structures disclose that the enzyme cannot accommodate cross-linked PG, explaining previous results showing that LytB is unable to digest purified cell walls (cross-linked glycan strands) from pneumococcal strains.[14] Collectively, our data provide a comprehensive understanding of LytB activity and document the need for the engagement of another PG hydrolase to remove cross-linked stem peptides prior to catalysis by LytB. The pneumococcus produces several PG peptidases, including the well-characterized LytA and PcsB enzymes,[19,20] but also others of unknown functions (Spr0168, Spr1875). The identification of this enzyme highlights the paucity of information that is now required to understand further the steps before LytB-mediated separation of daughter cells.

CBPs, the most important group of surface proteins in pneumococci and related bacteria, are involved in crucial aspects of the cellular cycle, such as fitness, virulence, host-pathogen interactions, or cell division.[9] These proteins share a specialized CBM that establishes multiple interactions with the PCho moieties that decorate TA for anchoring to the cell wall. However, many questions remain unanswered, notably, regarding the role of CBRs exhibiting important variations of the consensus sequence. Here, we answer this question for LytB. Indeed, we have shown that the three-dimensional structure of LytB$_{CBM}$ displays a distribution of repeats that defines three subdomains, each endowed with different properties and separated by a unique type of repeats observed only in LytB so far and that act as hinge regions (Figure 1A). Interestingly, sequence analysis of LytB reveals that this three-subdomain division of the CBM is preserved in pneumococci and related *S. mitis* and *S. oralis* (Figure S6E), pointing to a conserved function for each subdomain and, notably, that the N subdomain represents an evolved modification of a choline-binding domain that loses its main ability to anchor the cell wall to specifically recognize the PASTA 4 repeat of the kinase StkP. The same is true for the extracellular domain of StkP. Phylogenetic analyses have shown that the extracellular domain of StkP and homologs in streptococci is made of different types (A, B, and C types) of PASTA domains.[10] A striking feature is that the distal PASTA always belongs to the C-type category. In addition, the taxonomic distribution of LytB matched with the presence of the C-type PASTA motif required for the interaction with LytB.[10] Therefore, co-evolution of the N and M subdomains and distal PASTA would be part of a universal regulatory mechanism of the last step of cell division conserved in all streptococci.

Our studies document that the C subdomain is responsible for cell-wall attachment of LytB via specific recognition of WTA and that the NM subdomains are specifically involved in the interaction with the distal PASTA4 domain of the division regulatory protein kinase StkP (Figure 6A).[10] With this organization, the catalytic domain of LytB can be erected up to 400 Å from the membrane. This architecture is consistent with the cell-wall measurements made for the related species *Streptococcus gordonii*.[21] Indeed, the thickness of the periplasmic space (also

termed the inner wall zone [IWZ], 160 Å) and that of the mature PG (also termed outer wall zone [OWZ], 264 Å) are similar to that of the extracellular domain of StkP (150 Å) and LytB (240 Å). Our structure-function analysis further provides a comprehensive model for the spatiotemporal regulation of LytB activity (Figure 6B). Although it has been known that LytB catalyzes hydrolysis of PG at the very late stage of the cell-division process, it remained obscure as to how it is regulated to not induce aberrant cell lysis and is specifically active only at the end of the cell cycle. Our work provides the answer at the molecular level, demonstrating the coordinated functions of WTAs and StkP in anchoring LytB in the PG layer and in localization of LytB at the division septum, respectively. Furthermore, our findings show that LTA does not participate in binding of LytB to the cell wall and only WTA does (Figure 4C). However, the composition of the TA unit in WTA and LTA is identical in the pneumococcus, which brings focus to the means of anchoring in each case. It is proposed that LTA cannot penetrate into the PG layer and would maintain a kind of periplasmic space through the electrostatic repulsion with the WTAs that are projected toward the plasma membrane.[22,23] As WTAs represent 90% of total TAs,[24] those that project straight out on the external sides of the PG layer are available to interact with LytB. These data are thus consistent with our observations and our model proposing that LytB would be progressively propelled toward the external layer of the PG wall. Together with the flexibility provided by the linker between the CBM and the catalytic domain, this allows the progressive hydrolysis of septal PG, leading to the final separation of the two daughter cells (Figure 6B). Considering that LytB is recognized as a virulence factor involved in different aspects of host infection[25–27] and that the pneumococcus is on the WHO list of priority pathogens for research and development of new antibiotics,[28] our work holds the promise of providing a structural basis for the rational design of new drugs to combat pneumococcal infections.

Limitations of the study

Our strategy has allowed us to decipher the molecular interplay between the serine/threonine-kinase StkP and the PG hydrolase LytB to control the final separation of daughter cells during cell division. However, we have disclosed some residues that are crucial for the interaction that were confirmed both *in vitro* and *in vivo*, but we did not obtain the experimental three-dimensional structure of the complex, and it could be possible that other interacting residues from both proteins were also involved. Another limitation might be the lack of information on the stoichiometry of the StkP/LytB complex and the requirement of some other partners. Previous studies have shown that StkP homologs are able to form dimers and that their extracellular domain can interact with other proteins and with PG itself. Furthermore, LytB can process only non-reticulated glycan strands, suggesting that another peptidase or amidase should process PG first before LytB. Thus, our work should be extended in the future to investigate the molecular organization of a potential multiprotein complex using appropriate methods such as cryoelectron microscopy. Another interesting observation is that WTAs, but not LTAs, are also key. However, LTAs and WTAs have the same composition. Therefore, we still do not understand why
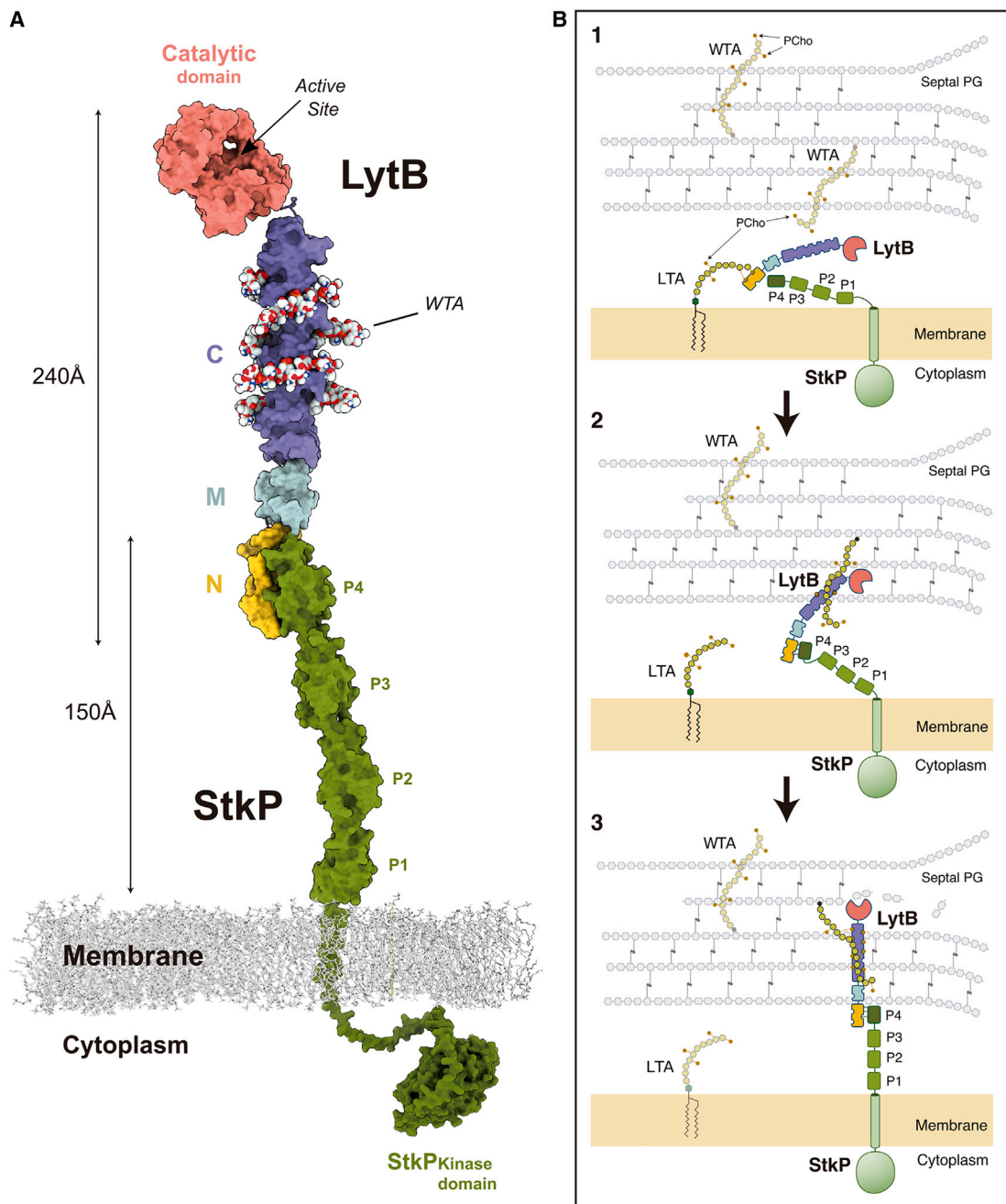
Figure 6. Model of StkP-LytB interaction and control of the final cell division step in streptococci

(A) Proposed model of LytB interaction with teichoic acids and StkP. While the C subdomain ensures the binding of LytB to the cell wall by winding around the wall teichoic acids decorated with phosphorylcholine, the NM subdomains drive the localization at the division septum through the interaction with the distal PASTA4 domain of StkP. With this organization, the catalytic domain of LytB can be sequestered up to 400 Å from the membrane surface. The StkP model was generated using AlphaFold2.

(B) A model of PG turnover performed by LytB and StkP at the final step of cell division is shown in the cartoon. Upon the export of LytB, the NM subdomains interact with the distal PASTA4 of StkP to position LytB at the division septum (step 1). Concomitantly, the C domain of LytB is wrapped by the wall teichoic acids protruding from the peptidoglycan layer (step 2). These interactions, together with the flexible nature of both the LytB$_{CBM}$ and the extracellular domain of StkP, allow the LytB catalytic domain to be erected across and toward the surface of the peptidoglycan layer. The linker between the catalytic domain and the CBM of LytB allows its positioning in different orientations to allow appropriate hydrolysis of the peptidoglycan.

LytB does not bind LTA or why LytB localization is not affected in the absence of LTA. Knowing that our knowledge of the dynamics of LTA and WTA assembly is limited, it will be crucial to track the LTA and WTA biosynthesis sites during cell division, possibly using click chemistry and superresolution imaging, and to decipher the molecular dialogue with LytB. This will also require the ability to produce fluorescent LytB from its chromosomal locus rather than adding it exogenously.

STAR★METHODS

Detailed methods are provided in the online version of this paper and include the following:

- KEY RESOURCES TABLE
- RESOURCE AVAILABILITY
  - Lead contact
  - Materials availability
  - Data and code availability
- EXPERIMENTAL MODEL AND STUDY PARTICIPANT DETAILS
  - Strains and growth conditions
- METHOD DETAILS
  - Construction of strains and plasmids
  - Protein production and purification
  - Phase contrast and fluorescence microscopy
  - Microscale thermophoretic analyses (MST)
  - Crystallization
  - Structure determination, model building and refinement
  - Small-angle X-ray scattering (SAXS) data collection, processing and modeling
  - Synthesis of the PG derivative
  - Molecular dynamics simulations
  - Ligand-protein and protein-protein docking
- QUANTIFICATION AND STATISTICAL ANALYSIS

AUTHOR CONTRIBUTIONS

S.M.-C., R.M., and S.G.B. performed crystallization. S.M.-C. and R.M. solved all the structures. C.F. together with C.M. conducted the molecular biology experiments, C.F. performed the cell imaging and pneumococcal genetics and

purified all the proteins for crystallographic studies. C.F. and V.G.-C. conducted the microscale thermophoresis experiments. K.V.M., M.L., D.H., and S.M. performed molecular dynamics simulations, analyzed results, and synthesized NAG_2NAM_2. S.M.-C., C.F., R.M., S.G.B., J.A.H., and C.G. designed and analyzed the data. C.G. and J.A.H. wrote the manuscript, and all authors reviewed and edited the text.

DECLARATION OF INTERESTS

The authors declare no competing interests.

INCLUSION AND DIVERSITY

We support inclusive, diverse, and equitable conduct of research.

REFERENCES

1. Fisher, J.F., and Mobashery, S. (2015). Bacterial cell wall: Morphology and biochemistry. In Practical Handbook of Microbiology, Third Edition (Taylor & Francis), pp. 221–264. https://doi.org/10.1201/b17871.

2. Page, J.E., and Walker, S. (2021). Natural products that target the cell envelope. Curr. Opin. Microbiol. *61*, 16–24. https://doi.org/10.1016/j.mib.2021.02.001.

3. Reichmann, N.T., Tavares, A.C., Saraiva, B.M., Jousselin, A., Reed, P., Pereira, A.R., Monteiro, J.M., Sobral, R.G., VanNieuwenhze, M.S., Fernandes, F., and Pinho, M.G. (2019). SEDS–bPBP pairs direct lateral and septal peptidoglycan synthesis in Staphylococcus aureus. Nat. Microbiol. *4*, 1368–1377. https://doi.org/10.1038/s41564-019-0437-2.

4. Grangeasse, C. (2016). Rewiring the Pneumococcal Cell Cycle with Serine/Threonine- and Tyrosine-kinases. Trends Microbiol. *24*, 713–724. https://doi.org/10.1016/j.tim.2016.04.004.

5. Fleurie, A., Lesterlin, C., Manuse, S., Zhao, C., Cluzel, C., Lavergne, J.P., Franz-Wachtel, M., MacEk, B., Combet, C., Kuru, E., et al. (2014). MapZ marks the division sites and positions FtsZ rings in Streptococcus pneumoniae. Nature *516*, 259–262. https://doi.org/10.1038/nature13966.

6. Garcia, P.S., Simorre, J.P., Brochier-Armanet, C., and Grangeasse, C. (2016). Cell division of Streptococcus pneumoniae: think positive. Curr. Opin. Microbiol. *34*, 18–23. https://doi.org/10.1016/j.mib.2016.07.014.

7. Sjodt, M., Rohs, P.D.A., Gilman, M.S.A., Erlandson, S.C., Zheng, S., Green, A.G., Brock, K.P., Taguchi, A., Kahne, D., Walker, S., et al. (2020). Structural coordination of polymerization and crosslinking by a SEDS–bPBP peptidoglycan synthase complex. Nat. Microbiol. *5*, 813–820. https://doi.org/10.1038/s41564-020-0687-z.

8. de Las Rivas, B., García, J.L., López, R., and García, P. (2002). Purification and polar localization of pneumococcal LytB, a putative endo-β-N-acetyl-glucosaminidase: The chain-dispersing murein hydrolase. J. Bacteriol. *184*, 4988–5000. https://doi.org/10.1128/JB.184.18.4988-5000.2002.

9. Galán-Bartual, S., Pérez-Dorado, I.,G.P., and H.J.A.. (2015). Structure and functions of choline binding proteins. ISBN: 978-0-12-410530-0. In Streptococcus Pneumoniae Molecular Mechanisms of Host-Pathogen Interactions, S. H.. and C.O. Jeremy Brown, eds. (Elsevier), pp. 207–230.

10. Zucchini, L., Mercy, C., Garcia, P.S., Cluzel, C., Gueguen-Chaignon, V., Galisson, F., Freton, C., Guiral, S., Brochier-Armanet, C., Gouet, P., and Grangeasse, C. (2018). PASTA repeats of the protein kinase StkP interconnect cell constriction and separation of Streptococcus pneumoniae. Nat. Microbiol. *3*, 197–209. https://doi.org/10.1038/s41564-017-0069-3.

11. Bai, X.H., Chen, H.J., Jiang, Y.L., Wen, Z., Huang, Y., Cheng, W., Li, Q., Qi, L., Zhang, J.R., Chen, Y., and Zhou, C.Z. (2014). Structure of pneumococcal peptidoglycan hydrolase LytB reveals insights into the bacterial

cell wall remodeling and pathogenesis. J. Biol. Chem. *289*, 23403–23416. https://doi.org/10.1074/jbc.M114.579714.

12. Lipski, A., Hervé, M., Lombard, V., Nurizzo, D., Mengin-Lecreulx, D., Bourne, Y., and Vincent, F. (2015). Structural and biochemical characterization of the β-N-acetylglucosaminidase from Thermotoga maritima: Toward rationalization of mechanistic knowledge in the GH73 family. Glycobiology *25*, 319–330. https://doi.org/10.1093/glycob/cwu113.

13. Pérez-Dorado, I., González, A., Morales, M., Sanles, R., Striker, W., Vollmer, W., Mobashery, S., García, J.L., Martínez-Ripoll, M., García, P., and Hermoso, J.A. (2010). Insights into pneumococcal fratricide from the crystal structures of the modular killing factor LytC. Nat. Struct. Mol. Biol. *17*, 576–581. https://doi.org/10.1038/nsmb.1817.

14. Rico-Lastres, P., Díez-Martínez, R., Iglesias-Bexiga, M., Bustamante, N., Aldridge, C., Hesek, D., Lee, M., Mobashery, S., Gray, J., Vollmer, W., et al. (2015). Substrate recognition and catalysis by LytB, a pneumococcal peptidoglycan hydrolase involved in virulence. Sci. Rep. *5*, 16198. https://doi.org/10.1038/srep16198.

15. Flores-Kim, J., Dobihal, G.S., Fenton, A., Rudner, D.Z., and Bernhardt, T.G. (2019). A switch in surface polymer biogenesis triggers growth-phase-dependent and antibiotic-induced bacteriolysis. Elife *8*, e44912. https://doi.org/10.7554/eLife.44912.

16. Heß, N., Waldow, F., Kohler, T.P., Rohde, M., Kreikemeyer, B., Gómez-Mejia, A., Hain, T., Schwudke, D., Vollmer, W., Hammerschmidt, S., et al. (2017). Lipoteichoic acid deficiency permits normal growth but impairs virulence of Streptococcus pneumonia. Nat. Commun. *8*. https://doi.org/10.1038/s41467-017-01720-z.

17. Asensio, J.L., Ardá, A., Cañada, F.J., and Jiménez-Barbero, J. (2013). Carbohydrate-aromatic interactions. Acc. Chem. Res. *46*, 946–954. https://doi.org/10.1021/ar300024d.

18. Tomasz, A. (1968). Biological consequences of the replacement of choline by ethanolamine in the cell wall of Pneumococcus: chanin formation, loss of transformability, and loss of autolysis. Proc. Natl. Acad. Sci. USA *59*, 86–93. https://doi.org/10.1073/pnas.59.1.86.

19. Sham, L.T., Barendt, S.M., Kopecky, K.E., and Winkler, M.E. (2011). Essential PcsB putative peptidoglycan hydrolase interacts with the essential FtsX Spn cell division protein in Streptococcus pneumoniae D39. Proc. Natl. Acad. Sci. USA *108*, E1061–E1069. https://doi.org/10.1073/pnas.1108323108.

20. Bartual, S.G., Straume, D., Stamsås, G.A., Muñoz, I.G., Alfonso, C., Martínez-Ripoll, M., Håvarstein, L.S., and Hermoso, J.A. (2014). Structural basis of PcsB-mediated cell separation in streptococcus pneumoniae. Nat. Commun. *5*, 3842. https://doi.org/10.1038/ncomms4842.

21. Zuber, B., Haenni, M., Ribeiro, T., Minnig, K., Lopes, F., Moreillon, P., and Dubochet, J. (2006). Granular layer in the periplasmic space of gram-positive bacteria and fine structures of Enterococcus gallinarum and Streptococcus gordonii septa revealed by cryo-electron microscopy of vitreous sections. J. Bacteriol. *188*, 6652–6660. https://doi.org/10.1128/JB.00391-06.

22. Erickson, H.P. (2021). How Teichoic Acids Could Support a Periplasm in Gram-Positive Bacteria, and Let Cell Division Cheat Turgor Pressure. Front. Microbiol. *12*, 664704–664711. https://doi.org/10.3389/fmicb.2021.664704.

23. Brown, S., Santa Maria, J.P., and Walker, S. (2013). Wall teichoic acids of gram-positive bacteria. Annu. Rev. Microbiol. *67*, 313–336. https://doi.org/10.1146/annurev-micro-092412-155620.

24. Briles, E.B., and Tomasz, A. (1973). Pneumococcal Forssman Antigen. J. Biol. Chem. *248*, 6394–6397. https://doi.org/10.1016/s0021-9258(19)43459-5.

25. Gosink, K.K., Mann, E.R., Guglielmo, C., Tuomanen, E.I., and Masure, H.R. (2000). Role of novel choline binding proteins in virulence of Streptococcus pneumoniae. Infect. Immun. *68*, 5690–5695. https://doi.org/10.1128/IAI.68.10.5690-5695.2000.

26. Ramos-Sevillano, E., Moscoso, M., García, P., García, E., and Yuste, J. (2011). Nasopharyngeal colonization and invasive disease are enhanced by the cell wall hydrolases LytB and LytC of Streptococcus pneumoniae. PLoS One *6*, e23626. https://doi.org/10.1371/journal.pone.0023626.

27. Rodriguez, J.L., Dalia, A.B., and Weiser, J.N. (2012). Increased chain length promotes pneumococcal adherence and colonization. Infect. Immun. *80*, 3454–3459. https://doi.org/10.1128/IAI.00587-12.

28. Tacconelli, E., Carrara, E., Savoldi, A., Harbarth, S., Mendelson, M., Monnet, D.L., Pulcini, C., Kahlmeter, G., Kluytmans, J., Carmeli, Y., et al. (2018). Discovery, research, and development of new antibiotics: the WHO priority list of antibiotic-resistant bacteria and tuberculosis. Lancet Infect. Dis. *18*, 318–327. https://doi.org/10.1016/S1473-3099(17)30753-3.

29. Sung, C.K., Li, H., Claverys, J.P., and Morrison, D.A. (2001). An rpsL Cassette, Janus, for Gene Replacement through Negative Selection in Streptococcus pneumoniae. Appl. Environ. Microbiol. *67*, 5190–5196. https://doi.org/10.1128/aem.67.11.5190-5196.2001.

30. Gibson, D.G., Young, L., Chuang, R.Y., Venter, J.C., Hutchison, C.A., and Smith, H.O. (2009). Enzymatic assembly of DNA molecules up to several hundred kilobases. Nat. Methods *6*, 343–345. https://doi.org/10.1038/nmeth.1318.

31. de Jong, I.G., Beilharz, K., Kuipers, O.P., and Veening, J.W. (2011). Live cell imaging of Bacillus subtilis and Streptococcus pneumoniae using automated time-lapse microscopy. J. Vis. Exp., e3145. https://doi.org/10.3791/3145.

32. Ducret, A., Quardokus, E.M., and Brun, Y.v. (2016). MicrobeJ, a tool for high throughput bacterial cell detection and quantitative analysis. Nat. Microbiol. *1*, 16077. https://doi.org/10.1038/nmicrobiol.2016.77.

33. Kabsch, W. (2010). Xds. Acta Crystallogr. D Biol. Crystallogr. *66*, 125–132. https://doi.org/10.1107/S0907444909047337.

34. Evans, P.R., and Murshudov, G.N. (2013). How good are my data and what is the resolution? Acta Crystallogr. D Biol. Crystallogr. *69*, 1204–1214. https://doi.org/10.1107/S0907444913000061.

35. Vonrhein, C., Tickle, I.J., Flensburg, C., Keller, P., Paciorek, W., Sharff, A., and Bricogne, G. (2018). Advances in automated data analysis and processing within autoPROC , combined with improved characterisation, mitigation and visualisation of the anisotropy of diffraction limits using STARANISO. Acta Crystallogr. A Found. Adv. *74*, a360. https://doi.org/10.1107/s010876731809640x.

36. McCoy, A.J., Grosse-Kunstleve, R.W., Adams, P.D., Winn, M.D., Storoni, L.C., and Read, R.J. (2007). Phaser crystallographic software. J. Appl. Crystallogr. *40*, 658–674. https://doi.org/10.1107/S0021889807021206.

37. Afonine, P.v., Grosse-Kunstleve, R.W., Echols, N., Headd, J.J., Moriarty, N.W., Mustyakimov, M., Terwilliger, T.C., Urzhumtsev, A., Zwart, P.H., and Adams, P.D. (2012). Towards automated crystallographic structure refinement with phenix.refine. Acta Crystallogr. D Biol. Crystallogr. *68*, 352–367. https://doi.org/10.1107/S0907444912001308.

38. Emsley, P., Lohkamp, B., Scott, W.G., and Cowtan, K. (2010). Features and development of Coot. Acta Crystallogr. D Biol. Crystallogr. *66*, 486–501. https://doi.org/10.1107/S0907444910007493.

39. Cowieson, N.P., Edwards-Gayle, C.J.C., Inoue, K., Khunti, N.S., Doutch, J., Williams, E., Daniels, S., Preece, G., Krumpa, N.A., Sutter, J.P., et al. (2020). Beamline B21: High-throughput small-angle X-ray scattering at Diamond Light Source. J. Synchrotron Radiat. *27*, 1438–1446. https://doi.org/10.1107/S1600577520009960.

40. Schneidman-Duhovny, D., Hammel, M., Tainer, J.A., and Sali, A. (2016). FoXS, FoXSDock and MultiFoXS: Single-state and multi-state structural modeling of proteins and their complexes based on SAXS profiles. Nucleic Acids Res. *44*, W424–W429. https://doi.org/10.1093/nar/gkw389.

41. Martínez-Caballero, S., Lee, M., Artola-Recolons, C., Carrasco-López, C., Hesek, D., Spink, E., Lastochkin, E., Zhang, W., Hellman, L.M., Boggess, B., et al. (2013). Reaction products and the X-ray structure of AmpDh2, a virulence determinant of Pseudomonas aeruginosa. J. Am. Chem. Soc. *135*, 10318–10321. https://doi.org/10.1021/ja405464b.

42. Mahasenan, K.v., Molina, R., Bouley, R., Batuecas, M.T., Fisher, J.F., Hermoso, J.A., Chang, M., and Mobashery, S. (2017). Conformational

dynamics in penicillin-binding protein 2a of methicillin-resistant staphylo-coccus aureus, allosteric communication network and enablement of catalysis. J. Am. Chem. Soc. *139*, 2102–2110. https://doi.org/10.1021/jacs.6b12565.

43. Cornell, W.D., Cieplak, P., Bayly, C.I., and Kollman, P.A. (1993). Application of RESP Charges To Calculate Conformational Energies, Hydrogen Bond Energies, and Free Energies of Solvation. J. Am. Chem. Soc. *115*, 9620–9631. https://doi.org/10.1021/ja00074a030.

44. Roe, D.R., and Cheatham, T.E. (2013). PTRAJ and CPPTRAJ: Software for processing and analysis of molecular dynamics trajectory data. J. Chem. Theor. Comput. *9*, 3084–3095. https://doi.org/10.1021/ct400341p.

45. Humphrey, W., Dalke, A., and Schulten, K. (1996). VMD: Visual molecular dynamics. J. Mol. Graph. *14*, 33–38. https://doi.org/10.1016/0263-7855(96)00018-5.

46. Denapaite, D., Brückner, R., Hakenbeck, R., and Vollmer, W. (2012). Biosynthesis of teichoic acids in Streptococcus pneumoniae and closely related species: Lessons from genomes. Microb. Drug Resist. *18*, 344–358. https://doi.org/10.1089/mdr.2012.0026.

47. Cortés-Cabrera, Á., Gago, F., and Morreale, A. (2015). A computational fragment-based de novo design protocol guided by ligand efficiency indices (LEI). In Methods in Molecular Biology, A.E. Klon, ed. (Springer New York), pp. 89–100. https://doi.org/10.1007/978-1-4939-2486-8_8.

48. Goodford, P.J. (1985). A Computational Procedure for Determining Energetically Favorable Binding Sites on Biologically Important Macromolecules. J. Med. Chem. *28*, 849–857. https://doi.org/10.1021/jm00145a002.

49. Kozakov, D., Hall, D.R., Xia, B., Porter, K.A., Padhorny, D., Yueh, C., Beglov, D., and Vajda, S. (2017). The ClusPro web server for protein-protein docking. Nat. Protoc. *12*, 255–278. https://doi.org/10.1038/nprot.2016.169.

50. Klett, J., Núñez-Salgado, A., dos Santos, H.G., Cortés-Cabrera, Á., Perona, A., Gil-Redondo, R., Abia, D., Gago, F., and Morreale, A. (2012). MM-ISMSA: An ultrafast and accurate scoring function for protein-protein docking. J. Chem. Theor. Comput. *8*, 3395–3408. https://doi.org/10.1021/ct300497z.

STAR★METHODS

KEY RESOURCES TABLE

REAGENT or RESOURCE	SOURCE	IDENTIFIER
Chemicals, peptides, and recombinant proteins		
100% PEG 300	Molecular Dimensions	Cat# MD2-100-2
1M Bis-Tris pH 6.5	Molecular Dimensions	Cat# MD2-004-PH
1M Calcium Acetate	Molecular Dimensions	Cat# MD2-100-39
1M Ammonium Acetate	Merck	Cat# 631-61-8
1M Bis-Tris propane pH 7.0	Molecular Dimensions	Cat# MD2-005-PH
50% PEG 6000	Molecular Dimensions	Cat# MD2-100-12
1M MES pH 6.5	Molecular Dimensions	Cat# MD2-013-PH
2M Zinc Chloride	Molecular Dimensions	Cat# MD2-250-96
Critical commercial assays		
JBScreen JCSG^{++}	Jena Bioscience	Cat# CS-151
SaltRx HT	Hampton Research	Cat# HR2-107 Cat# HR2-107
Gibson assembly	Home made	N/A
Monolith Protein Labeling kit RED-NHS	NanoTemper	Cat# MO-L011
Monolith Capillaries	NanoTemper	Cat# MO-K022
Deposited data		
Model of LytB$_{cat}$ closed	This paper	PDB: 7PL3
Model of LytB$_{cat}$ open	This paper	PDB: 7PJ3
Model of LytB$_{cat}$ E585Q	This paper	PDB: 7PJ4
Model of LytB$_{cat}$:NAG$_4$	This paper	PDB: 7PJ5
Model of LytB$_{cat}$-E585Q:1, 5 sites (-3, +2)	This paper	PDB: 7PJ6
Model of LytB$_{cat}$-E585Q:1, 4 sites (-3, +1)	This paper	PDB: 7POD
Model of LytB$_{NM}$	This paper	PDB: 7PL5
Model of LytB$_{CBM}$	This paper	PDB: 7PL2
Experimental models: Organisms/strains		
E.coli: BL21(DE3) Competent cells	Novagen	Cat# 69450-3
E.coli: AD494 Competent cells	Novagen	Cat# 69450-3
Oligonucleotides		
DNA primers	This paper	Table S5
Recombinant DNA		
Pt7-7-TEV-his6-LytB (various mutation)	This paper	Tables S4 and S5
Software and algorithms		
XDS	Kabsch et al., 2010	https://xds.mr.mpg.de/
Aimless	Evans et al., 2013	https://www.ccp4.ac.uk/html/aimless.html
autoPROC pipeline	Vonrhein et al., 2018	https://www.globalphasing.com/autoproc/
Phaser	McCoy et al., 2007	https://www.ccp4.ac.uk/html/phaser.html
PHENIX	Adams et al., 2010	https://phenix-online.org/
COOT	Emsley et al., 2010	https://www2.mrc-lmb.cam.ac.uk/personal/pemsley/coot/
FoXS	Schneidman-Duhovny et al., 2016	https://modbase.compbio.ucsf.edu/foxs/
PyMOL	The PyMOL Molecular Graphics System, Version 2.0 Schrödinger, LLC	https://pymol.org/2/
ChimeraX	Goddard et al., 2018	https://www.cgl.ucsf.edu/chimerax/
ImageJ	Schneider et al., 2012	http://rsb.info.nih.gov/ij/
MicrobeJ	Ducret et al., 2016	https://www.microbej.com/

Continued

REAGENT or RESOURCE	SOURCE	IDENTIFIER
AMBER 18	Case et al., 2014	https://ambermd.org/
RESP	Cornell et al., 1993	https://upjv.q4md-forcefieldtools.org/RED/resp/
CPPTRAJ	Roe et al., 2013	http://ambermd.org/AmberTools.php
VMD	Humphrey et al., 1996	https://www.ks.uiuc.edu/Research/vmd/
ClusPro Server	Kozakov et al., 2017	https://cluspro.bu.edu/login.php
MM-ISMSA	Klett et al., 2012	http://ub.cbm.uam.es/software/mmismsa.php
Monolith MO.Affinity Analysis Software	NanoTemper	Cat# MO-S001A
Other		
Amicon concentrators (30K)	Millipore	Cat# UFC903024
Ni-NTA agarose	Qiagen	Cat# 30210

RESOURCE AVAILABILITY

Lead contact
Further information and requests for resources and reagents should be directed to and will be fulfilled by the lead contact, Christophe Grangeasse (christophe.grangeasse@ibcp.fr).

Materials availability
All reagents generated in this study are available upon request to the lead contact with a completed Materials Transfer Agreement.

Data and code availability
- The atomic coordinates and structural factors included in this study have been deposited in the Protein Data Bank under the accession codes under the accession codes: LytB$_{cat}$ closed (PDB: 7PL3), LytB$_{cat}$ open (PDB: 7PJ3), LytB$_{cat}$ -E585Q (PDB; 7PJ4), LytB$_{cat}$:NAG4 (PDB: 7PJ5), LytB$_{cat}$ -E585Q:C1, 5 sites:-3 − +2 (PDB: 7PJ6), LytB$_{cat}$ -E585Q:C1, 4 sites:-3 − +1 (PDB: 7POD), CBM (R1-R9) (PDB: 7PL5) and CBM (PDB: 7PL2).
- This paper does not report original code.
- Any additional information required to reanalyze the data reported in this paper is available from the lead contact upon request.

EXPERIMENTAL MODEL AND STUDY PARTICIPANT DETAILS

Strains and growth conditions
Streptococcus pneumoniae R6, WT and mutants (Table S4) were cultured in Todd-Hewitt Yeast broth at 37°C. The PASTA4 repeat and LytB and derivatives were produced in *E. coli* BL21(DE3) or AD494 cells grown in Luria Bertani broth (LB). Growth was performed in presence of appropriated antibiotics and monitored in the JASCO V-630-BIOspectrophotometer by OD readings at 550 nm or 600 nm for *S. pneumoniae* or *E. coli* strains, respectively. To generate protoplasts, cells were further treated by lysozyme (0.5 mg/ml) a,d mutanolysin (25 U/ml) for 30 min at 37°C in 0.5 M sucrose, 20 mM maleic acid pH 6.5, 20 mM MgCl$_2$.

METHOD DETAILS

Construction of strains and plasmids
Pneumococcal mutant strains carrying either gene deletion, or mutation were constructed as previously described in[10] by homologous recombination using the based on the Janus cassette.[29] All gene modifications are performed at their native chromosomal locus in *S. pneumoniae*.

For the construction of plasmids overproducing LytB derivatives (alone or fused to the GFP) (Table S4), the DNA encoding the LytB domains of interest were PCR amplified using pneumococcal chromosomal DNA from the *S. pneumoniae* R800 strain as a template. Fusion of the *lytB* DNA fragments encoding LytB$_{cat}$, LytB$_{NM-cat}$ and LytB$_{C-cat}$ to the *gfp* and their insertion in the pT7-7 plasmid were performed by Gibson assembly.[30] The plasmid producing GFP-LytB full length was described in.[14]

For structure characterization and interaction studies, the DNA fragments coding for LytB domains (LytB$_{CBM}$, LytB$_{cat}$, LytB$_{cat-E585Q}$, LytB$_{NM}$, LytB$_{NM-cat}$ LytB$_N$, LytB$_{Nmut}$ and LytB$_C$, LytB$_{C-cat}$, were cloned between the NdeI and PstI cloning sites of pT7-7 modified in house with a TEV site (pT7-7-TEV). All plasmids and primers used for strain and plasmid constructions are presented in Tables S4 and S5, respectively. All plasmids and pneumococcal strains were verified by DNA sequencing to verify error-free PCR amplification.

Protein production and purification

LytB full length, GFP-LytB full length and PASTA 4 were purified as previously described in.[10] LytB domains (LytB$_{CBM}$, LytB$_{cat}$, LytB$_{cat-E585Q}$, LytB$_{NM}$, LytB$_{NM-cat}$ LytB$_N$, LytB$_{Nmut}$ and LytB$_C$, LytB$_{C-cat}$, including the GFP fused derivatives (GFP-LytB$_{cat}$, GFP-LytB$_{C-cat}$ and GFP-LytB$_{NM-cat}$), were purified using the 6 histidine-tag encoded by the pT7-7-TEV plasmid described above. Cells were grown at 37°C until OD600nm=0.6 and gene expression was induced with 0.1 mM IPTG overnight at 25°C. Cells were then harvested by centrifugation at 5,000 g for 10 min at 4°C and resuspended in buffer A (20 mM Tris-HCl pH 8, 100 mM NaCl, 10 mM imidazole) for LytB$_{cat}$, LytB$_{cat-E585Q}$ and GFP-LytB$_{cat}$ or in Buffer A' (20 mM Tris-HCl pH 8, 0.5M Choline, 10 mM imidazole) for LytB$_{CBM}$, LytB$_{NM}$, LytB$_{NM-cat}$, LytB$_N$, LytB$_{Nmut}$ and LytB$_C$, LytB$_{C-cat}$, GFP-LytB$_{C-cat}$ and GFP-LytB$_{NM-cat}$. Buffer A and A' were supplemented with 1 μg/ml of lysozyme, 1μg/ml of protease inhibitor and 6 μg/ml of DNase I /RNase A before use. After sonication and centrifugation 30 min at 30,000 g, the supernatant was applied to a Ni-NTA column and washed with buffer A or A'. Elution was then performed with buffer E1 (20 mM Tris-HCl pH 8, 100 mM NaCl, 300 mM imidazole) for LytB$_{cat}$, LytB$_{cat-E585Q}$ and GFP-LytB$_{cat}$, or Buffer E2 (20 mM Tris-HCl pH 8, 0.5M Choline, 300 mM imidazole) for LytB$_{NM}$, LytB$_{NM-cat}$, LytB$_N$, LytB$_{Nmut}$ and LytB$_{C-cat}$, GFP-LytB$_{C-cat}$ and GFP-LytB$_{NM-cat}$, or with Buffer E3 (20 mM Tris-HCl pH 8, 1M Choline, 300 mM imidazole) for LytB$_{CBM}$, and LytB$_C$. Eluted fractions were analyzed by SDS-PAGE and the fractions containing pure protein were pooled and dialyzed in the presence of the TEV protease overnight at 4°C in buffer D1 (20 mM Tris-HCl pH 8, 150 mM NaCl, 1 mM DTT, 0.5 mM EDTA) for LytB$_{cat}$, LytB$_{cat-E585Q}$ and GFP-LytB$_{cat}$, or Buffer D2 (20 mM Tris-HCl pH 8, 0.5M Choline, 1 mM DTT, 0.5 mM EDTA) for LytB$_{NM}$, LytB$_{NM-cat}$, LytB$_N$, LytB$_{Nmut}$ and LytB$_{C-cat}$, GFP-LytB$_{C-cat}$ and GFP-LytB$_{NM-cat}$, or with Buffer D3 (20 mM Tris-HCl pH 8, 1M Choline, 1 mM DTT, 0.5 mM EDTA) for LytB$_{CBM}$, and LytB$_C$. 0.025mg of TEV protein per mg of protein to cleave was added in the dialysis tubing. Then, proteins were applied again onto a Ni-NTA column in order to remove the TEV protease and non-cleaved proteins. Proteins without a 6 histidine-tag were then concentrated and stored at -80°C.

Phase contrast and fluorescence microscopy

Pneumococcal cells were grown until OD550 = 0.1/0.2 and visualized using a Nikon TiE microscope fitted with an Orca-CMOS Flash4 V2 camera with a 100 Å∼ 1.45 objective. For immunofluorescence microscopy, cells or protoplasts were mixed with purified GFP-LytB or derivatives (10 μg ml^{-1}) at 37 °C for 30 min and then imaged as described.[31] Images were collected using the NIS-Elements (Nikon) and analysed using the software ImageJ (http://rsb.info.nih.gov/ij/) and the plugin MicrobeJ[32] to generate the percentage of chain, fluorescent intensity heat maps and violin plots. These experiments were biologically and technically made in triplicates.

Microscale thermophoretic analyses (MST)

Binding experiments were carried out by microscale thermophoresis with a Monolith NT.115 Series instrument (Nano Temper Technologies). The 6His-PASTA4 domain was labelled using the Monolith Protein Labeling Kit RED-NHS according to the manufacturer's instructions. Briefly, 16 nM of labelled 6His-PASTA4 mixed (1:1 v/v) with increasing concentrations of either 6His-LytB$_{NM}$ (from 818 μM to 0.025 μM), 6His-LytB$_C$ (from 930 μM to 0.0284 μM), 6His-LytB$_N$ (from 1210 μM to 0.037 μM) or 6His-LytB$_{Nmut}$ (from 326 μM to 0.00994 μM μM) were loaded into standard Monolith NT.115 capillaries and MST was measured at RT in buffer 20mM Tris HCl pH8, 0.5M Choline, 1mM DTT, 0.5mM EDTA, 0.1 % Tween 20. Analysis was performed with the Monolith software. The dissociation constant (Kd) to measure affinity was quantified by analysing the change in the fraction bound as a function of the ligand concentration. In order to calculate the fraction bound, all ΔFnorm (normalized fluorescence = fluorescence after thermophoresis/ initial fluorescence) values of a curve are divided by the curve amplitude, resulting in the fraction bound (from 0 to 1) for each data point. These experiments were biologically and technically made in triplicates.

Crystallization

Crystallization screenings were performed by high-throughput techniques in a Nanodrop robot (Innovadyne Technologies Inc.) and screening using JBScreen PACT^{++}, JBScreen Classic 1 to 4 and JBScreen JCSG^{++} 1 to 4 (Jena Bioscience), Crystal Screen, Crystal Screen 2, SaltRx HT and Index HT (Hampton Research) and Wizard Cryo (Rigaku). Positive conditions in which crystals grew were optimized by the sitting-drop vapor diffusion method at 290 K by mixing 1 μL of protein solution and 1 μL of precipitant solution, equilibrated against 150 μL of precipitant solution in the reservoir chamber. Crystals of catalytic domain and the mutant E585Q were obtained at a concentration of 13 mg/mL in 46% PEG 300, 100 mM Bis-Tris pH 6.5 and 200 mM calcium acetate. The complex with the peptidoglycan derivate DH166 and the N, N', N'', N'''-Tetraacetylchitotetraose were obtained by co-crystallization trials, the compounds were diluted at a final concentration of 5 mM using the crystallization condition described above and mixing 1 μl of this solution and 1 μl of protein. Crystals of choline-binding module plus the linker (N, M, C subdomains +linker) were obtained at a concentration of 8 mg/mL in 3.2 M ammonium acetate and 0.1 M Bis-Tris propane pH 7.0. Crystals of choline-binding module (R1-R9) were obtained at a concentration of 5 mg/mL in 24% PEG 6000, 100 mM MES pH 6.5 and 10 mM zinc chloride and the crystals of choline-binding module (R1-R7) were obtained at a concentration of 13.5 mg/mL in 2.8 M sodium acetate pH 7.0 and 0.1 M Bis-Tris propane pH 7.5.

Structure determination, model building and refinement

Diffraction data sets were collected in beamline XALOC at the ALBA synchrotron (Barcelona, Spain) and processed using XDS[33] and Aimless[34] from CCP4 program suite. Choline-binding module (R1-R7) diffraction pattern presented anisotropy that was corrected by

using the STARANISO server (http://staraniso.globalphasing.org/cgi-bin/staraniso.cgi) with a surface threshold of Local mean I/sd (I) of 2.5, implemented through the autoPROC pipeline.[35] Structures were solved by molecular replacement method using Phaser.[36] The peptidoglycan hydrolase (PDB: 4Q2W) was used as template to the catalytic domain, the X was used as template to the choline-binding module (R1-R9), the choline-binding domain CbpL (PDB: 4CNL) and the refined model of choline-binding module (R1-R9) obtained by us (PDB: 7PL5) were used as template to solve the structure of the choline-binding module plus the linker (N, M, C subdomains +linker) and finally these last structure was used as template to the choline-binding module (R1-R7). The Refinement and manual models building were performed with Phenix[37] and Coot[38] respectively. Data collection and processing statistics are shown in Tables S1 and S2.

Small-angle X-ray scattering (SAXS) data collection, processing and modeling

SAXS experiments were performed at the beamline B21 of the Diamond Light Source (Didcot, UK).[39] A sample of 40 ul of LytB at concentration of 4 mgml-1 were delivered at 20ºC via an in-line Agilent 1200 HPLC system in a Superdex 200 Increase 3.2 column, using a running buffer composed by 20mM Tris pH = 8.0 and 500 mM choline. The continuously eluting samples were exposed for 300s in 10s acquisition blocks using an X-ray wavelength of 1 Å, and a sample to detector (Eiger 4M) distance of 3.7 m. The data covered a momentum transfer range of $0.0032 < q < 0.34$ Å^{-1}. The frames recorded immediately before elution of the sample were subtracted from the protein scattering profiles. The Scåtter software package (www.bioisis.net) was used to analyse data, buffer-subtraction, scaling, merging and checking possible radiation damage of the samples. The R_g value was calculated with the Guinier approximation assuming that at very small angles $q < 1.3/R_g$. The particle distance distribution, D_{max}, was calculated from the scattering pattern with GNOM, and shape estimation was carried out with DAMMIF/DAMMIN, all these programs included in the ATSAS package (Petoukhov). The proteins molecular mass was estimated with GNOM. Interactively generated PDB-based homology models were made using the program COOT[38] by manually adjusting the X-ray structures obtained in this work, into the envelope given by SAXS until a good correlation between the real-space scattering profile calculated for the homology model matched the experimental scattering data. This was computed with the program FoXS.[40]

Synthesis of the PG derivative

ß-methyl NAG-NAM-NAG-NAM (compound 1) was prepared according to the literature method developed by our laboratory.[41]

Molecular dynamics simulations

The X-ray structure of the catalytic and CBD domains were linked to each other with a modelled sequence (A444-E447), which formed part of the nine-residue loop that connects the CBD to the catalytic domain (G441-A449). The conformation of the linker was manually generated using the Maestro program (v 2019-4) and connected the X-ray structures of the catalytic domain and CBD repeat. This initial full-length model was immersed in a rectangular box of TIP3P waters, energy minimized, and subjected to MD simulation for 20 ns using the *pmemd* module of AMBER 18, following a previously described protocol.[42] AMBER ff14SB and GAFF provided forcefield parameters, while charges for choline molecules were calculated with the RESP methodology.[43] The flexible linker sampled multiple conformations allowing motion of the catalytic domain around the CBD. Snapshots from this initial MD provided various linker conformations. The linker loop conformations formed the basis for modelling four full-length LytB structures suitable for final MD on a longer time scale. The four models of full-length LytB (Figure S1) were generated orienting the catalytic domain in different directions. The models were further subjected to the MD simulation protocol for a total period of 400 ns (100 ns each). The MD simulations explored a wider conformational landscape. The MD trajectories were analysed with *cpptraj*[44] and VMD[45] programs.

Ligand-protein and protein-protein docking

The unique zwitterionic chain structures of pneumococcal LTA and WTA,[46] together with the large number of cavities −both deep and shallow− and solvent-exposed hydrophobic surfaces in LytB, pose major challenges to automated docking programs. We first generated affinity maps using selected chemical probes[47,48] and then followed a divide-and-conquer approach to identify feasible binding orientations in both canonical and non-canonical choline binding sites (CBS and NCBS, respectively) for a diversity of fragments, including phosphorylcholine (PCho), methyl phosphorylcholine, and di-, tri- and tetrasaccharides, both in the presence and absence of ribitol-phosphate (RboP). The stability and convergence of the resulting poses was then assessed by running MD simulations of the ensuing complexes as described above.

A tentative/feasible model for the association of LytB with the fourth and membrane-distal PASTA domain 4 of the protein kinase StkP (PASTA4) was built by following the efficient fast Fourier transform correlation approach implemented in the ClusPro server[49] and defining LytB as the receptor and PASTA4 (PDB: 5NOD)[10] as the ligand. This automated protein-protein docking method involves rigid-body docking and scoring followed by root-mean-squared-deviation-based clustering and refinement by means of energy minimization. Importantly, it considers not only shape complementarity (with some tolerance to steric overlap) but also electrostatic and desolvation contributions. A top-ranked solution from the set of models generated using a van der Waals plus electrostatic energy scheme juxtaposed the distinctive charged and surface-exposed patch (R633A, E636A, K642A, R644A and K646A) present at the bottom of the three-stranded β-sheet of PASTA4 with pocket 2 of the N-terminal domain of LytB, which is lined by the side chains of K54, E55, D56, and E63. The stability of this complex was assessed by running MD simulations in an aqueous medium

under periodic boundary conditions, as described above, and the binding energy was calculated and decomposed into residue contributions with the aid of the MM-ISMSA program.[50]

QUANTIFICATION AND STATISTICAL ANALYSIS

Quantification and statistical analysis of microscopy experiments were performed using Microbe J[32] and GraphPad Prism (https://www.graphpad.com/). Statistical tests and details can be found in the figure legends.

Supplemental information

Molecular basis of the final step of cell

division in *Streptococcus pneumoniae*

Siseth Martínez-Caballero, Céline Freton, Rafael Molina, Sergio G. Bartual, Virginie Gueguen-Chaignon, Chryslène Mercy, Federico Gago, Kiran V. Mahasenan, Inés G. Muñoz, Mijoon Lee, Dusan Hesek, Shahriar Mobashery, Juan A. Hermoso, and Christophe Grangeasse

SUPPLEMENTAL INFORMATION TITLES AND LEGENDS
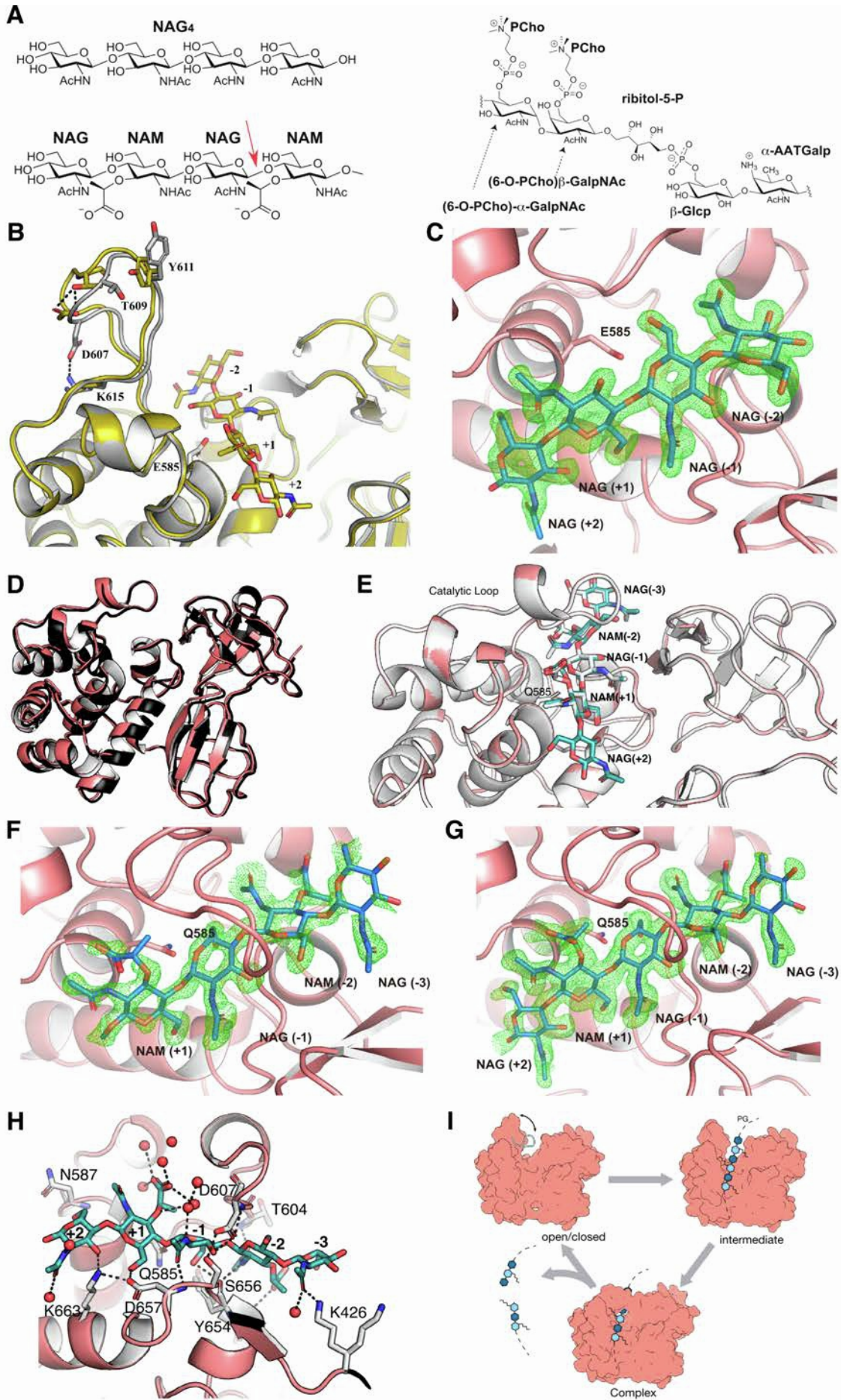
Figure S1 to Figure S6

Tables S1 to S5

Video SI1: Simulated molecular dynamics trajectory of LytB in complex with one phosphorylcholine (first part) or phosphorylethanolamine (second part) molecule bound to each CBS.

Video SI2: Molecular dynamic simulations over 400 ns showing the linker flexibility and different orientations adopted by the catalytic module versus de CBM.
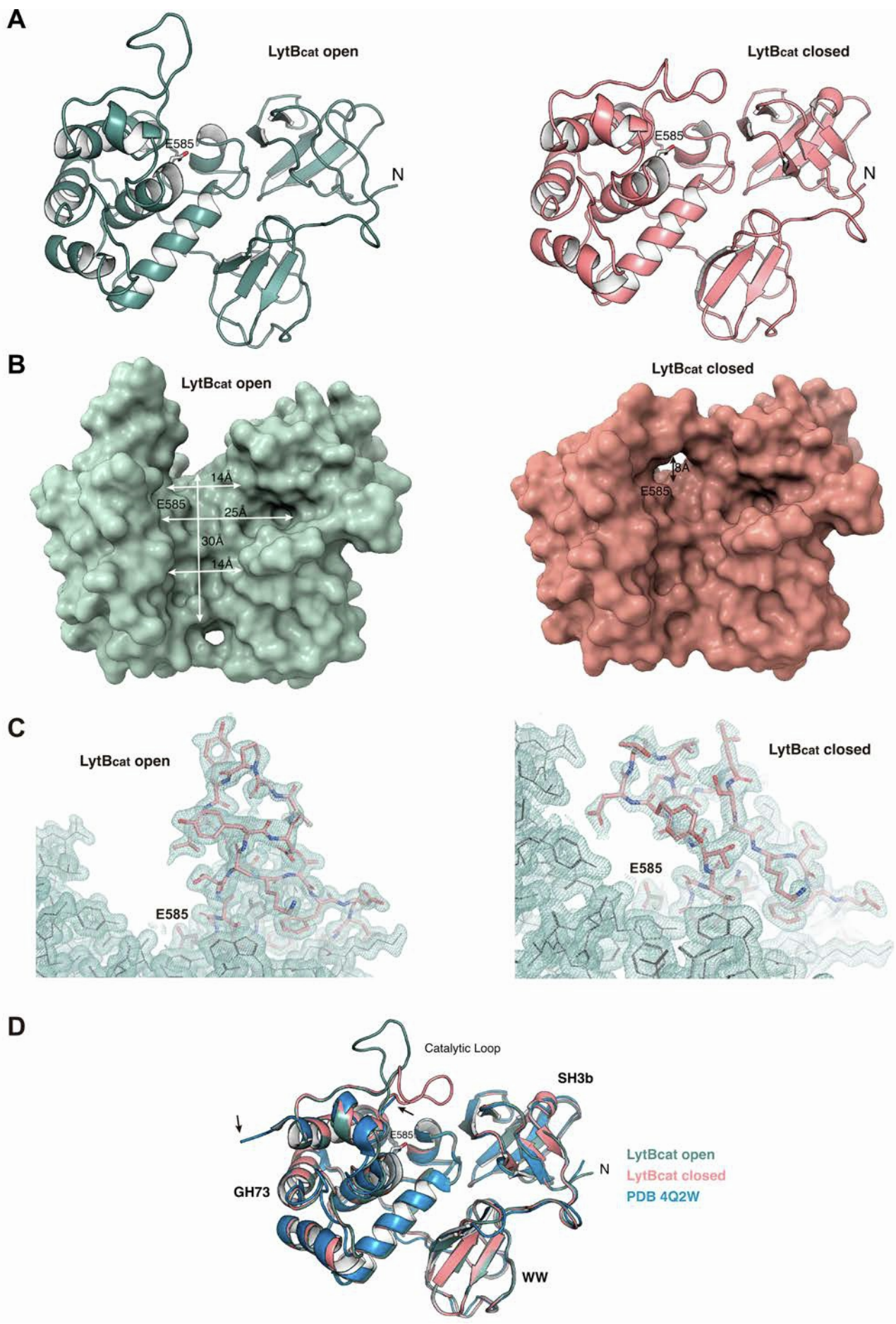
Figure S1. Apo LytBcat structures. (A) Cartoon representation of the open (green) and closed (salmon) conformations. (B) Molecular surface for the LytBcat open and LytBcat closed displaying the dimensions of the substrate-binding site. Position of the catalytic E585 residue is indicated. (C) Electron density map (2Fo-Fc map contoured at 0.8 σ) for the catalytic loop region in open (left panel) and closed (right panel) conformation. In panels (A) and (B) the salmon sticks represent the amino acids of loop and in stick gray the catalytic glutamic. (D) Structural superimposition of LytBcat open, LytB closed and PDB 4Q2W (blue). The observed extremes of the catalytic loop in 4Q2W are indicated by arrows. Catalytic residue depicted as capped sticks and labeled. Domains in the catalytic module of LytB are labeled.

A
NAG4

NAG   NAM   NAG   NAM

PCho
PCho
ribitol-5-P
(6-O-PCho)β-GalpNAc
(6-O-PCho)-α-GalpNAc
α-AATGalp
β-Glcp

B
Y611
T609
D607
K615
E585
-2
-1
+1
+2

C
E585
NAG (-2)
NAG (-1)
NAG (+1)
NAG (+2)

D

E
Catalytic Loop
NAG(-3)
NAM(-2)
NAG(-1)
Q585
NAM(+1)
NAG(+2)

F
Q585
NAM (-2)   NAG (-3)
NAG (-1)
NAM (+1)

G
Q585
NAM (-2)   NAG (-3)
NAG (-1)
NAM (+1)
NAG (+2)

H
N587
D607
T604
+2
+1
-1
-2
-3
K663
Q585
S656
D657
Y654
K426

I
PG
open/closed
intermediate
Complex

Figure S2. Substrate triggers closing of the catalytic loop. (A) Chemical structures of pneumococcal peptidoglycan and synthetic analogues. Upper left panel, drawing of the peptidoglycan analogue chemical formula: N′, N′′, N′′′, N′′′′-Tetraacetylchitotetraose. Down left panel, drawing of the peptidoglycan synthetic Compound **1** (NAG-NAM-NAG-NAM-OCH3) chemical formula (red arrow indicates the bond cleaved by LytB). Right panel, chemical formula of the pneumococcal teichoic acid repeating unit. (B) Zoom view showing the conformational change in the catalytic loop upon interaction with the NAG_4 ligand. The $LytB_{cat}$ open conformation is shown as gray cartoon and the $LytB_{cat}$:NAG_4 complex as yellow cartoon. Relevant residues involved in the interaction pattern are depicted as capped sticks and labeled. The NAG_4 ligand drawn as capped sticks and subsites numbered. (C) Electron density map (Fo-Fc omit map contoured at 3.0 σ) for the tetraacetylchitotetraose. (D) Superimposition of LytBcat WT (black) into LytBcatE585Q (salmon). (E) Structural superimposition of $LytB_{cat}$-E585Q:1 complexes showing two poses for the ligand. In one of the complexes the NAG-NAM-NAG-NAM tetrasaccharide spans from site -3 to site +1 (white cartoon and ligand as white sticks). In the other crystal we observed two populations for the ligand, both occupying sites -1 and +1, one of them from site -3 to +1 (as previous one) and the other population from site -1 to +3 (electron density for site +3 was of poor quality and was not modeled). This second complex is represented as salmon cartoon and with the ligand as green sticks. (F) Electron density map (Fo-Fc omit map contoured at 3.0 σ) for the compound 1 occupying the -3 to +1 sites. (G) Electron density map (Fo-Fc omit map contoured at 3.0 σ) for the compound 1 distributed in two populations occupying the -3 to +2 sites. The substrate analogues are represented in blue sticks. (H) Zoom view showing the residues and the network of water molecules stabilizing PG substrate at the active site of LytB. Relevant residues depicted as capped sticks and labeled. Positions for the substrate sugars are numbered, hydrolytic cleavage produced between position -1 (NAG) and +1 (NAM). Water molecules represented as red spheres. (I) Model of peptidoglycan recognition mechanism by LytB. Open/closed states for the catalytic loop where here observed in the absence of substrate. An intermediate state (catalytic loop with an intermediate conformation between open and closed) was observed in the NAG4 complex. To cleave the glycosidic bond connecting NAG and NAM moieties, catalytic loop presents a close conformation trapping the substrate near the catalytic E585 residue.
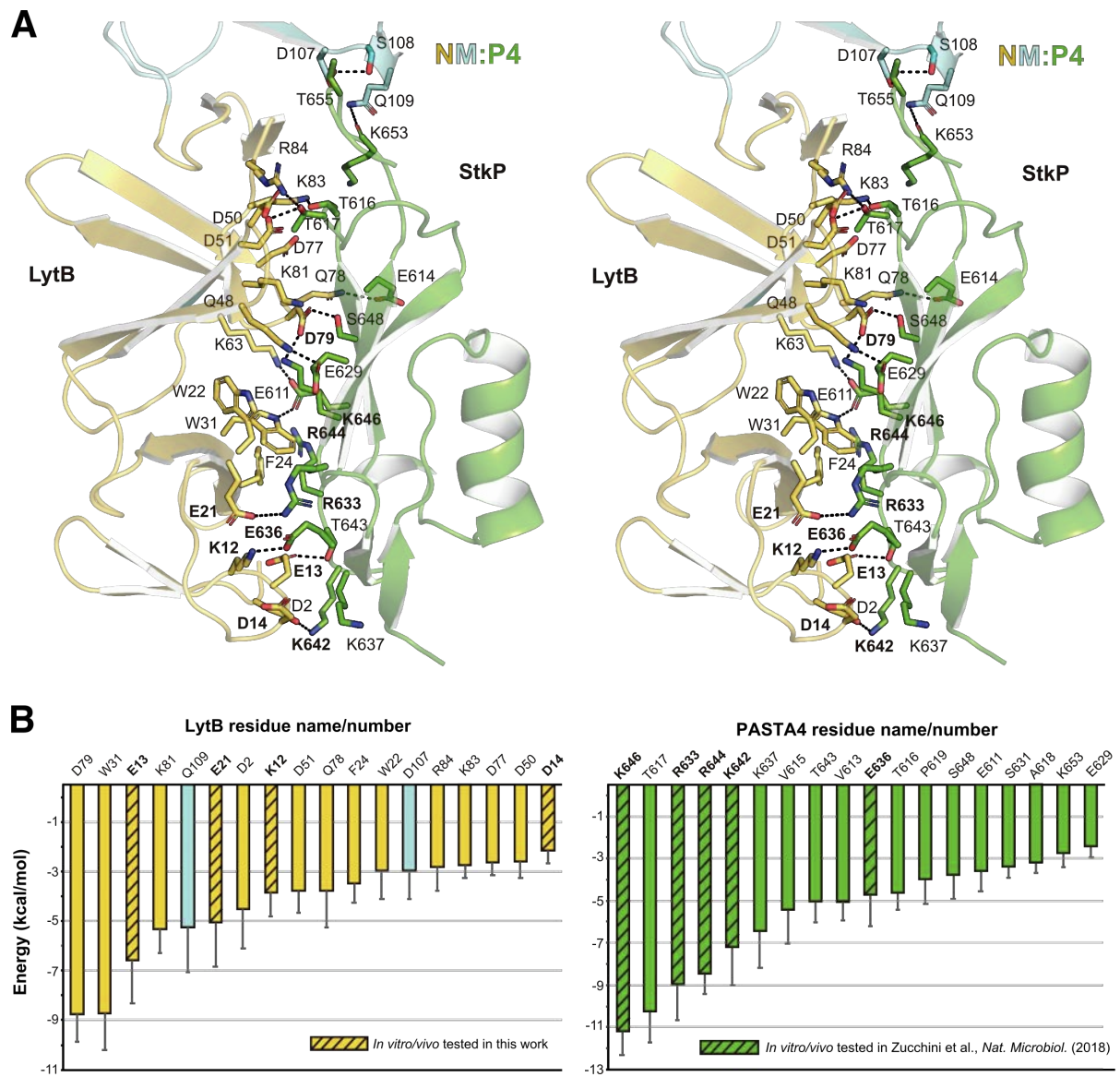
Figure S3. Interaction network between StkP-PASTA4 and LytB-NM. (A) Stereo view model of predicted StkP-PASTA4:LytB-NM interactions from MD simulations. StkP-PASTA4 (green) and LytB subdomains N (dark yellow) and M (light blue) displaying its key interacting residues in sticks. In bold, key interacting residues shown in Figure 5A. (B) Solvent-corrected interaction energies between LytB:PASTA4 throughout the MD simulations. These per-residue interaction binding energies, which together represent a "binding fingerprint", were calculated by means of program MM-ISMSA [50] using LytB as the receptor and PASTA4 as the ligand (left) or PASTA4 as the receptor and LytB as the ligand (right). Average values (± standard errors, kcal mol^{-1}) were obtained from an ensemble of 60 complex structures from the MD simulations after equilibration (5-300 ns), cooling down to 273 K and energy minimization. A cut-off of 2.0 kcal mol^{-1} was used in the plots for enhanced clarity. Shadowed bars indicate in vitro/vivo mutants tested in LytB (this work) or tested in PASTA4 (Zucchini et al Nat. Microbiol 2018).

A

B
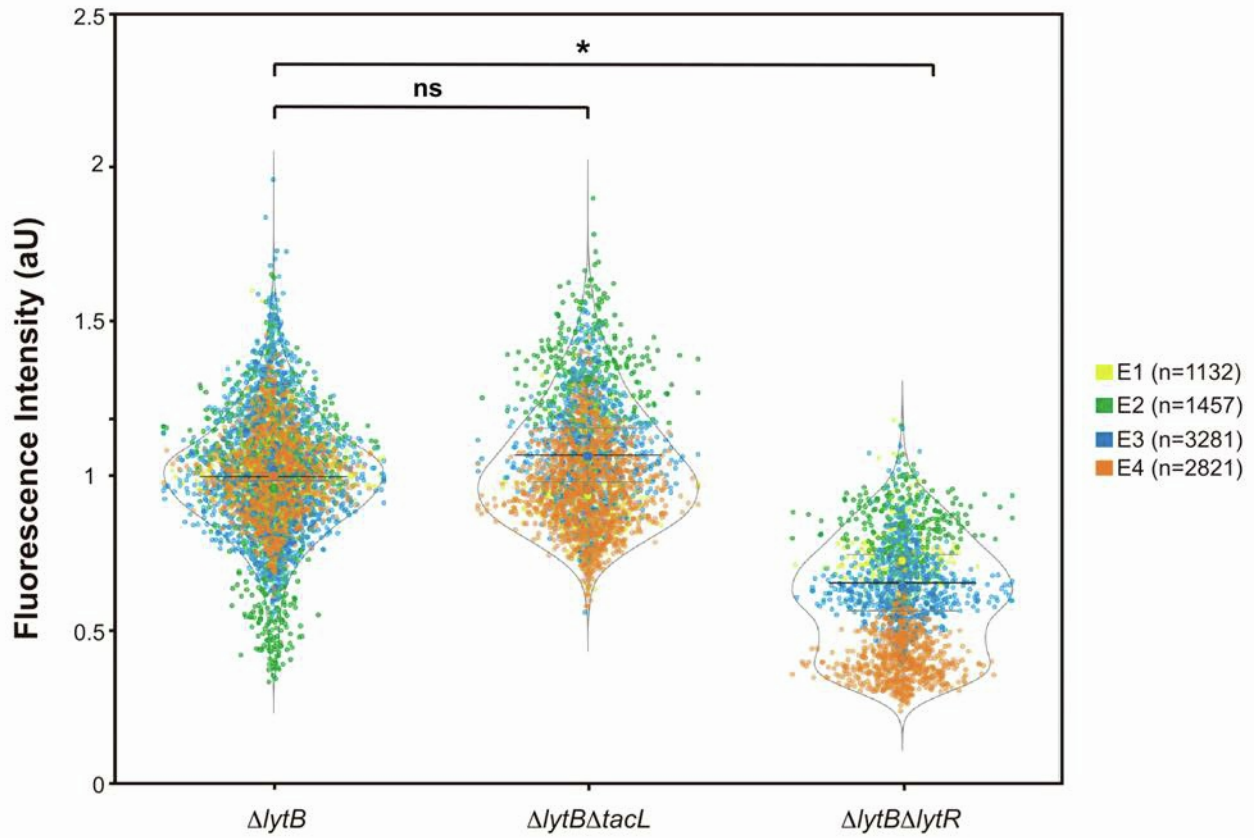
### ΔlytBΔtacL cells + GFP-LytB_{C-cat}
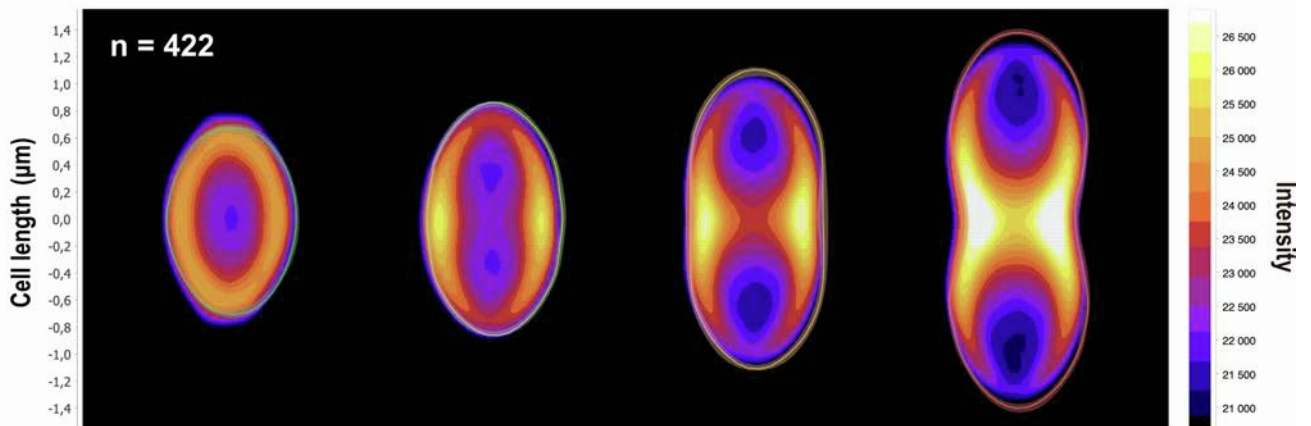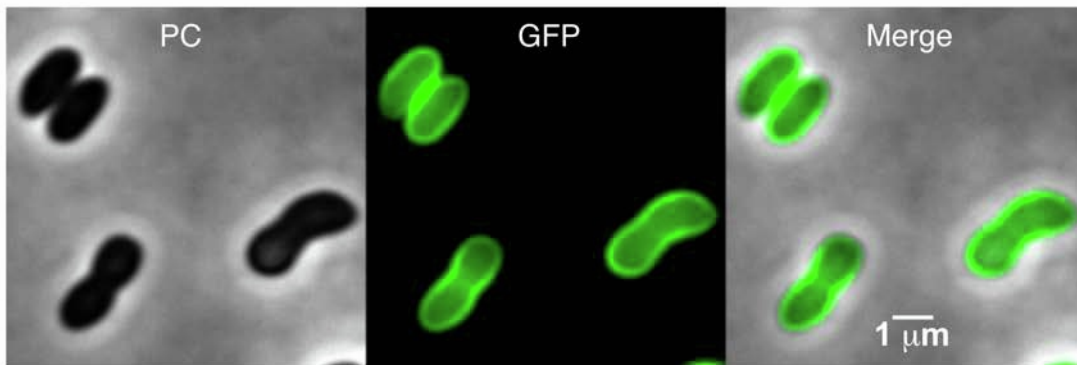
Figure S4. Binding of GFP-LytB$_{C-cat}$ to Δ*lytB*, Δ*lytB*Δ*tacL* and Δ*lytB*Δ*lytR* cells. (A) Total fluorescence of GFP-LytB$_{C-cat}$ bound to Δ*lytB*, Δ*lytB*Δ*tacL* or Δ*lytB*Δ*lytR* cells. The figure shows super-violin plot with data from 4 independent experiment shown in yellow, green, blue and orange. The error bar, the data points and the black horizontal line represent the s.e.m, the median of each experiment and the mean of the 4 experiments, respectively. Data from Δ*lytB*Δ*tacL* and Δ*lytB*Δ*lytR* cells are normalized to Δ*lytB* data taken as 1. Statistical comparison was done using t-test. *P<0.05 and ns, not significant P>0.05. **(B)** Δ*lytB*Δ*tacL* cells were treated with GFP–LytB$_{C-cat}$ and then imaged. Phase contrast (PC, left), GFP fluorescent signal (middle) and overlays (right) are shown; scale bar, 1 μm. The corresponding heat maps representing the localization patterns of GFP–LytB$_{C-cat}$ are shown on the right. The n value represents the number of cells analysed in a single representative experiment made in triplicate.
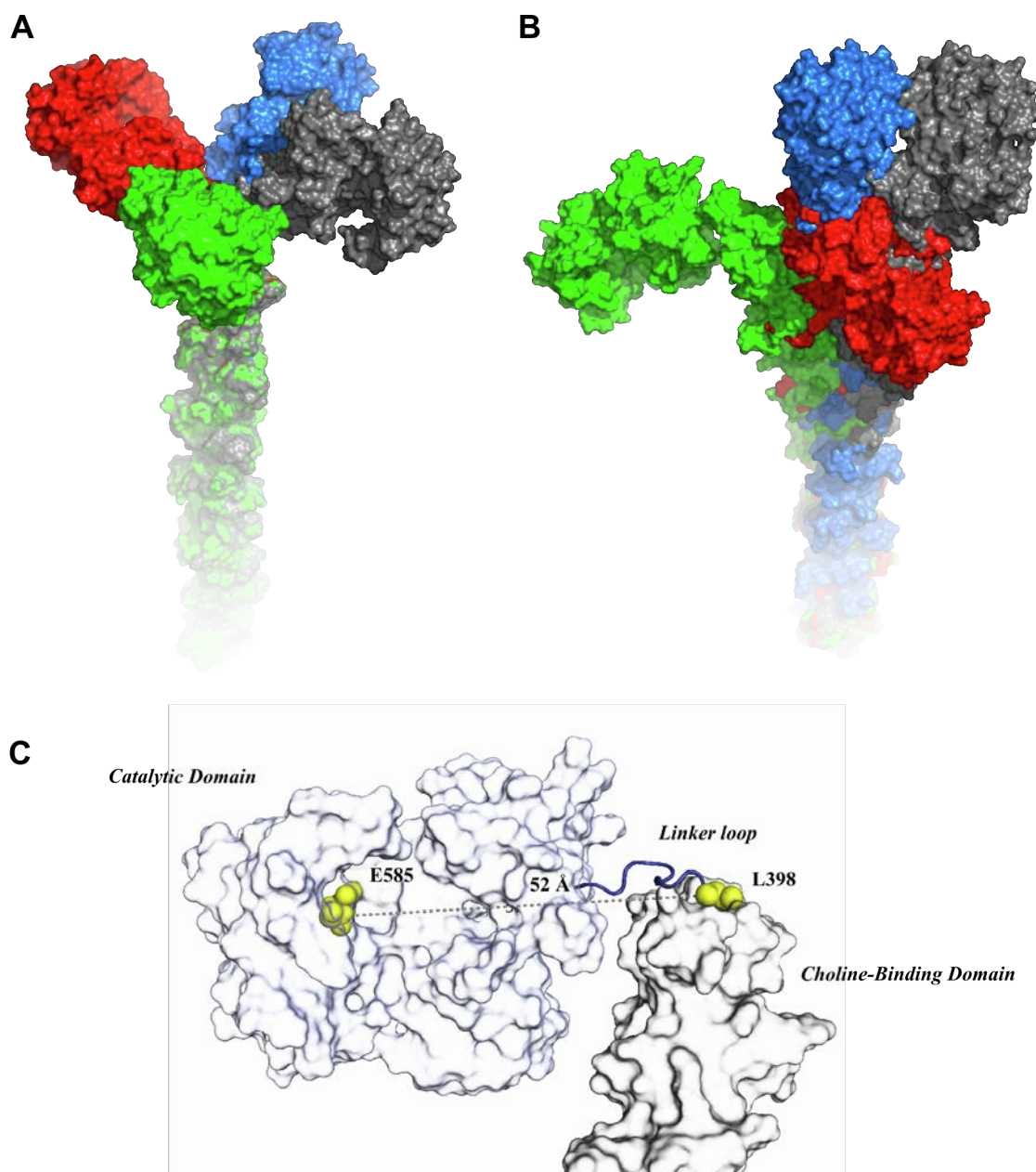
Figure S5. MD simulations on LytB full length models. (A) Superimposition of the four full-length LytB models generated based on different linker loop conformations. Each of the models, displayed in surface representation, are differentially colored. The N-terminus is towards the bottom of the image, which leads to the membrane-anchored region of LytB. The models provided starting conformations of MD simulations. (B) LytB conformations, each obtained from MD simulation of full-length LytB models (different colors). Simulations suggest a wide reach of the catalytic site around the CBD. c, Snapshot from MD simulation shows that the linker loop by itself allows the catalytic site to reach a region of about 50-Å radius from the CBD C-terminus. The catalytic domain and CBD are

in translucent surface representation in blue and gray, respectively, while the loop is depicted as a wire in purple. The distance from the Cα of residue L398 (nearly the centroid of the CBD axis) to the Cα of E585 (catalytic Glu) is 52 Å and is displayed in a gray broken line.
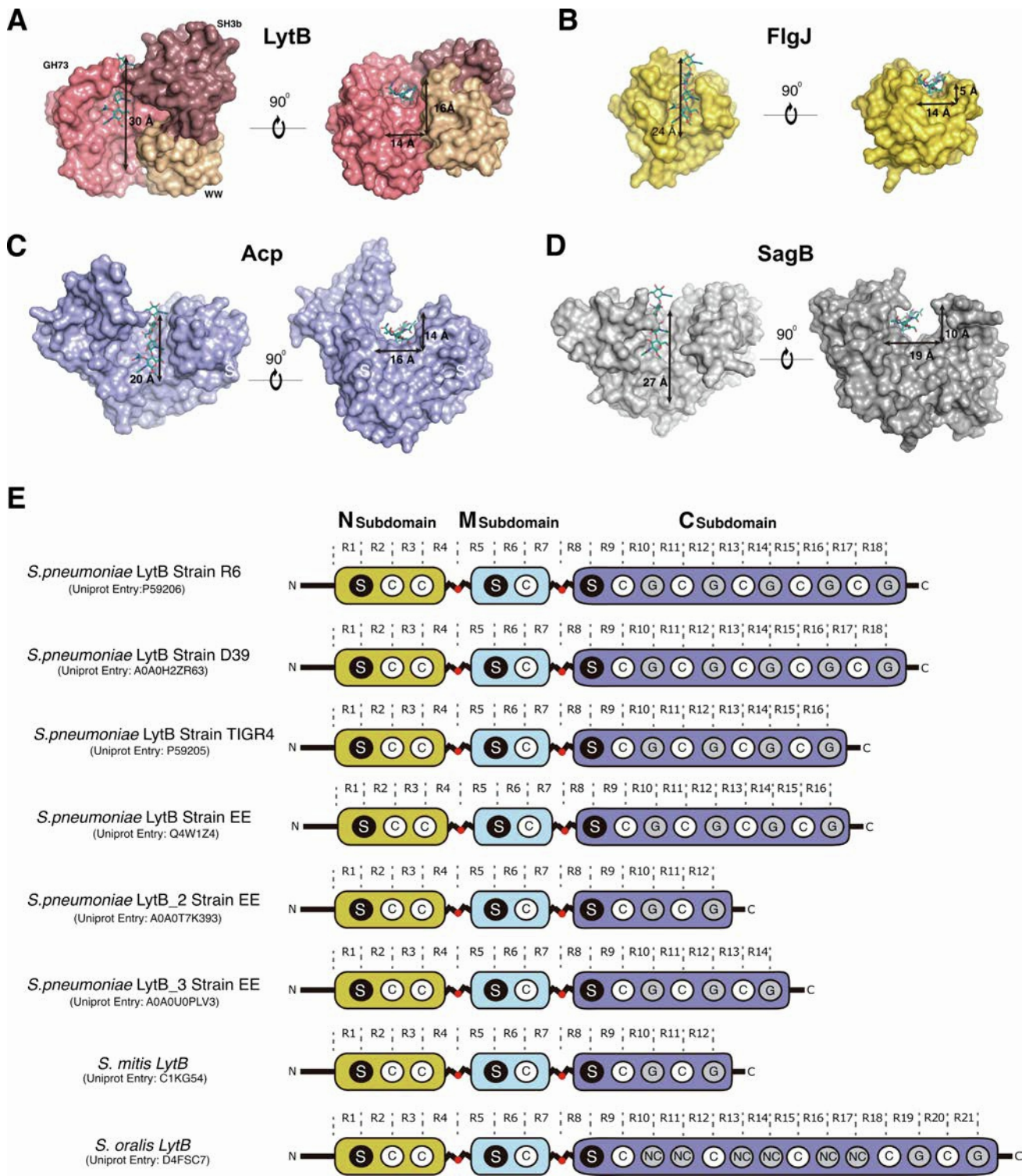
Figure S6. Structural homology of LytB catalytic domain and sequence variability of the Choline-binding Domains. (A-D) Substrate binding cavities of the LytB catalytic domain vs its structural homologues. Surface representations of the *S. pneumoniae* LytB catalytic domain in

complex with its substrate (**A**) (PDB code: 4Q2W); FlgJ from *Thermotoga maritina* (PDB code:4QDN) (**B**); Acp from *Clostridium prefringens* (PDB code:5WQW) (**C**); and SagB from *Staphylococcus aureus* (PDB code:6FXP) (**D**). For comparison reasons, LytB substrate is docked onto FlgJ, Acp and SagB substrate binding cavities. (**E**) Sequence variability between different LytB variants at their Choline-Binding Domains. Distribution of the LytB choline-binding sites along the choline-binding module of different LytB variants. Starting, Canonical and GYMA choline-binding sites are depicted as S, C and G, respectively. In *S. oralis*, some different non-canonical (NC) sites were predicted by sequence analysis.

17

Table S1. Crystallographic data for the catalytic domain of LytB

	LytB$_{cat}$ closed	LytB$_{cat}$ open	LytB$_{cat}$-E585Q	LytB$_{cat}$:NAG$_4$	LytB$_{cat}$-E585Q:1 5 sites (-3,+2)	LytB$_{cat}$-E585Q:1 4 sites (-3,+1)
Data collection statistics						
Wavelength (Å)	0.979263	0.979263	0.979260	0.979260	0.979260	0.979260
Space group	C 2 2 2$_1$	C 2 2 2$_1$	C 2 2 2$_1$	C 2 2 2$_1$	C 2 2 2$_1$	C 2 2 2$_1$
Unit cells dimensions *a, b, c* (Å) α,β,γ (°)	47.16,92.68,124.56 90,90,90	47.28, 92.61,124.39 90,90,90	46.65,92.68,124.20 90,90,90	47.68,92.36,124.30 90,90,90	47.29,92.54,124.79 90,90,90	47.14,92.52,124.57 90,90,90
Temp (K)	100	100	100	100	100	100
Resolution range (Å)	43.43-1.78 (1.82-1.78)	46.31-1.43 (1.45-1.43)	46.34-1.25 (1.27-1.25)	46.18-1.55 (1.58-1.55)	46.27-1.30 (1.32-1.30)	46.26-1.50 (1.53-1.50)
Unique reflections	26519 (1491)	50892 (2479)	74735 (3690)	40276 (1981)	67551 (3302)	43792 (2156)
Completeness (%)	99.7 (99.9)	100 (100)	100 (100)	100 (100)	99.9 (99.6)	99.5 (100)
Multiplicity	5.6 (5.5)	13.1 (13.4)	12.0 (12.2)	12.8 (13.1)	13.0 (12.5)	9.9 (10.1)
R$_{merge}$	0.093(0.763)	0.040(0.775)	0.066(0.763)	0.058(0.701)	0.065 (0.765)	0.048 (0.660)
R$_{pim}$	0.042 (0.354)	0.012 (0.219)	0.020(0.226)	0.017 (0.199)	0.019 (0.222)	0.016 (0.217)
CC1/2	0.998 (0.855)	1.0 (0.926)	0.999 (0.903)	0.999 (0.951)	0.999 (0.929)	1.0 (0.933)
$\langle I/\sigma (I) \rangle$	11.5 (1.9)	31.0 (3.6)	20.4 (3.9)	24.5 (4.9)	19.6 (3.2)	24.0 (3.9)
Refinement statistics						
Resolution range (Å)	43.43-1.8	43.40-1.43	43.42-1.25	43.29-1.55	43.39-1.3	43.37-1.5
Rwork/Rfree	0.172/0.182	0.144/0.185	0.136/0.162	0.143/0.192	0.150/0.175	0.145/0.194
No. atoms						
Protein	2212	2255	2288	2226	2267	2242
Water	138	181	301	160	224	172
Ligand	31	41	38	88	115	92
Root-Mean-Square Deviations						
Bond length (Å)	0.018	0.014	0.013	0.014	0.015	0.015
Bond angles (deg)	1.99	1.71	1.62	1.73	1.73	1.73
Ramachandran Favored/outliers (%)	97.05/0	96.68/0	97.05/0	96.31/0	97.05/0	97.42/0
Residues in the AU	273	273	273	273	273	273
Average B-factor	26.32	24.53	16.40	25.53	22.41	23.92
Macromolecules	25.70	23.40	14.56	24.74	21.02	22.77
Ligand	34.44	37.14	26.13	27.00	26.16	32.28
Solvent	34.31	35.81	29.19	35.76	34.59	34.49
PDB code	7PL3	7PJ3	7PJ4	7PJ5	7PJ6	7POD

Highest-resolution shell statistics are in parentheses

Table S2. Crystallographic data for the choline-binding module of LytB

	LytB$_{NM}$	LytB$_{CBM}$
Data collection statistics		
Wavelength (Å)	0.979260	0.979312
Space group	P 1 2$_1$ 1	P 6
Unit cells dimensions *a, b, c* (Å) α, β, γ (°)	45.30, 96.14, 49.10 90, 100.97, 90	202.10, 202.10, 26.47 90,90,120.0
Temp (K)	100	100
Resolution range (Å)	48.20-1.99 (2.03-1.99)	48.54-2.98 (3.16-2.98)
Unique reflections	28181 (1665)	12892 (2036)
Completeness (%)	98.7 (83.5)	97.1 (97.7)
Multiplicity	5.5 (3.9)	2.3 (2.4)
R$_{merge}$	0.238 (0.952)	0.151 (0.621)
R$_{pim}$	0.108 (0.496)	0.117 (0.467)
CC1/2	0.983 (0.634)	0.974 (0.527)
$<I/\sigma (I)>$	6.0 (2.1)	4.2 (1.5)
Refinement statistics		
Resolution range (Å)	44.47-1.99	43.76-2.98
Rwork/Rfree	0.172/0.233	0.219/0.272
No. atoms		
Protein	3042	3405
Water	212	26
Ligand	98	119
Root-Mean-Square Deviations		
Bond length (Å)	0.017	0.013
Bond angles (deg)	1.98	1.30
Ramachandran Favored/outliers (%)	98.04/0	92.68/0.25
Residues in the AU	361	415
Average B-factor	26.71	68.10
Macromolecules	25.96	68.08
Ligand	45.10	72.94
Solvent	28.99	48.49
PDB code	7PL5	7PL2

Highest-resolution shell statistics are in parentheses

Table S3. SAXS Data Collection and derived parameters for LytB

Data collection parameters	
Instrument	Diamond Light Source beamline B21 (Harwell Campus, UK)
Wavelength (Å)	1
q-range (Å^{-1})	0.0032–0.38
Exposure time (s)	300
Concentration (mg ml^{-1})	4
Temperature (K)	293
Structural parameters	
Protein	LytB
Rg (Å) (from Guinier)	71.83±0.08
Rg (Å) (from P(r))	72.25±0.08
Dmax (Å)	288±0.2
Molecular mass determination	
MM (kDa) from Porod volume	101
Calculated MM (kDa) from sequence	79.32
Software employed	
Data processing	Scåtter/PRIMUS/ GNOM
Ab initio analysis / Averaging	DAMMIF, DAMMIN/DAMAVER
Computation of model intensities	FoXS
3D graphics representations	PyMOL

Table S4. Strains and plasmids

#	Strains name	Génotype and description	References	# Primers table
1	R800	*S. pneumoniae* R6 derivative strain	Gift from JP Claverys (Toulouse-France)	
2	WT	R800 *rpsL1* (Str^R)	*Fleurie et al. , 2012*	
3	*ΔlytB::kan-rpsL*	R800 *rpsL1 ; ΔlytB::kan-rpsL* (Str^S ; Kan^R)	*Zuchinni et al. , 2018*	
4	*ΔlytB*	R800 *rpsL1 ; ΔlytB* (Str^R)	*Zuchinni et al. , 2018*	
5	*lytB-GH73-E$_{585}$A*	R800 *rpsL1 ; lytB E585A* (Str^R)	This study	3 , 4 , 5 and 6
6	*lytB-GH73-E$_{585}$Q*	R800 *rpsL1 ; lytB E585Q* (Str^R)	This study	3, 4 and 7
7	*lytB-SH3b-K$_{426}$E*	R800 *rpsL1 ; lytB K426E* (Str^R)	This study	3, 4 and 8
8	*lytB-GH73-Y$_{635}$A*	R800 *rpsL1 ; lytB Y635A* (Str^R)	This study	3, 4 and 9
9	*lytB-GH73-3Mut*	R800 *rpsL1 ; lytB Y654A - S656A - D657K* (Str^R)	This study	3, 4 and 10
10	*lytB-GH73-2Mut*	R800 *rpsL1 ; lytB Y606A - D607K* (Str^R)	This study	3, 4 and 13
11	*lytB-WW-5Mut*	R800 *rpsL1 ; lytB Y477A - E479K - Y486A - Y488A - Y511A* (Str^R)	This study	3, 4, 11, 12 and 14
12	*lytB-ΔN*	R800 *rpsL1 ; lytB ΔCBR1-3* (Str^R)	This study	16, 17, 24 and 34
13	*lytB-ΔM*	R800 *rpsL1 ; lytB ΔCBR6-8* (Str^R)	This study	18, 19, 24 and 34
14	*lytB-ΔC*	R800 *rpsL1 ; lytB ΔCBR9-18* (Str^R)	This study	20, 21, 24 and 34
15	*lytB-ΔNΔM*	R800 *rpsL1 ; lytB ΔCBR1-7* (Str^R)	This study	22, 23, 24 and 34
16	*lytB-Nmut*	R800 *rpsL1 ; lytB K12A – E13A – D14A – E21A* (Str^R)	This study	3, 4 and 15
17	*ΔlytR::kan-rpsL*	R800 *rpsL1 ; ΔlytR::kan-rpsL* (Str^S, Kan^R)	This study	1, 2, 39, 40, 41 and 42
18	*ΔlytR*	R800 *rpsL1 ; ΔlytR* (Str^R)	This study	39, 40, 43 and 44
19	*ΔlytR , ΔlytB::kan-rpsL*	R800 *rpsL1 ; ΔlytR , ΔlytB::kan-rpsL* (Str^S ; Kan^R)	This study	3 and 4
20	*ΔlytR , ΔlytB*	R800 *rpsL1 ; ΔlytR , ΔlytB* (Str^R)	This study	3 and 4
21	*ΔlytB , ΔtacL::kan-rpsL*	R800 *rpsL1 ; ΔlytB , ΔtacL::kan-rpsL* (Str^S ; Kan^R)	This study	1, 2, 45, 46, 47 and 48
22	*ΔlytB , ΔtacL*	R800 *rpsL1 ; ΔlytB , ΔtacL* (Str^S ; Kan^R)	This study	45, 46, 49 and 50
23	*stkP-ΔPASTA4*	R800 *rpsL1 ; stkp-ΔPASTA4* (Str^R)	*Zuchinni et al. , 2018*	
24	*stkP-ΔPASTA4, ΔlytB::kan-rpsL*	R800 *rpsL1 ; stkp-ΔPASTA4, ΔlytB::kan-rpsL* (Str^S ; Kan^R)	This study	3 and 4
25	*stkP-ΔPASTA4, ΔlytB*	R800 *rpsL1 ; stkp-ΔPASTA4, ΔlytB* (Str^R)	This study	3 and 4
26	LytB	pT7.7 - *lytB*	*Zuchinni et al. , 2018*	
27	LytB$_{cat}$	pT7.7 - *lytB cat*	This study	28 and 32
28	LytB$_{cat\ E585Q}$	pT7.7 - *lytB cat E585Q*	This study	7, 28 and 32
29	LytB$_{CBM}$	pT7.7 - *lytB CBR1-18-linker*	This study	25 and 30
30	LytB$_N$	pT7.7 - *lytB CBR1-4*	This study	26 and 33
31	LytB$_{Nmut}$	pT7.7 - *lytB CBR1-4 K12A – E13A – D14A – E21A*	This study	15, 26, and 33
32	LytB$_{NM}$	pT7.7 - *lytB CBR1-8*	This study	26 and 31
33	LytB$_C$	pT7.7 - *lytB CBR8-18-linker*	This study	27 and 30
34	LytB$_{NM-cat}$	pT7.7 - *lytB CBR1-8-linker-cat*	This study	26 and 32
35	LytB$_{C-cat}$	pT7.7 - *lytB CBR8-18-linker-cat*	This study	27 and 32
36	GFP-LytB	pT7.7 - *GFP - lytB*	Gift from Pedro Garcia	
37	GFP-LytB$_{cat}$	pT7.7 - *GFP - lytB cat*	This study	29, 32, 35 and 37
38	GFP-LytB$_{NM-cat}$	pT7.7 - *GFP - lytB CBR1-8-linker-cat*	This study	29, 32, 35, and 36
39	GFP-LytB$_{C-cat}$	pT7.7 - *GFP - lytB CBR8-18-linker-cat*	This study	29, 32, 35, and 38
40	GFP-LytB$_{Nmut}$	pT7.7 - *GFP - lytB (Full length and mutated K12A/E13A/D14A/E21A)*	This study	29, 32, 35, and 36

Table S5. Primers

#	Primer Name	+/-	Sequence 5'->3'
1	5'- [kan-rpsL]	+	CCGTTTGATTTTTAATGGATAATG
2	3' - [kan-rpsL]	-	AGAGACCTGGGCCCCTTTCC
3	upstream region lytB	+	GCAGCTGTTTCTCATGG
4	downstream region lytB	-	CCAACCTATCATGATTGCGC
5	lytB E585A	-	CCCCAGTTACTGGCTAGGGCACTATGGGC
6	lytB E585A	+	GCCCATAGTGCCCTAGCCAGTAACTGGGG
7	lytB E585Q	+	GCCCATAGTGCCCTACAAAGTAACTGGGGAAG
8	lytB K426E	+	CAGATGGTGAAGAGCTTTCCTATATATCGC
9	lytB Y635A	+	GGATTAAGGAAAATGCTATCGATAGGGG
10	lytB Y654A - S656A - D657K	+	GGTATGAATGTGGAAGCTGCTGCAAAACCTTATTGGGGCG
11	lytB Y486A - Y488A	+	GGCCACCGTTTTGCTCACGCTGTGGCTCAGAATGC
12	lytB Y511A	+	GGCAAGAAATATGCTTCGGCAGATGGCC
13	lytB Y606A - D607K	+	GGCATTACAGCCGCTAAAACGACCCCTTACC
14	lytB Y477A-E479A-Y486A-Y488A	+	GCGCTAGATGCTAGTAAGGACTTTATCCCTGCTTATAAGAGTGATGGCCACCGTTTTGCTCACGCTGTGGCTCAGAATGC
15	lytB K12A-E13A-D14A-E21A	+	GGAAAACAGTATCTGGCAGCAGCTGGCAGTCAAGCAGCGAATGCGTGGGTTTTTGATAC
16	**5' lytB CBR4** / lytB CBM up	-	**CCTTGTCTTCTACCCATTCTGA**AGCCATTGCACCCTCTGG
17	**lytB CBM up** / 5' lytB CBR4	+	**CCAGAGGGTGCAATGGCT**TCAGAATGGGTAGAAGACAAGG
18	**5' lytB CBR9** / 3' lytB CBR5	-	**TTTGTCAAAAAGCCAACCTTG**TATTACTTTGGCACCTGTTGC
19	**3' lytB CBR5** / 5' lytB CBR9	+	**GCAACAGGTGCCAAAGTAATA**CAAGGTTGGCTTTTTGACAAA
20	**lytB CBR18 down** / 3' lytB CBR8	-	**GATAACCATCTACTGTCTCATT**CTGTACTTTGGCACCACTAG
21	**3' lytB CBR8** / lytB CBR18 down	+	**CTAGTGGTGCCAAAGTACAG**AATGAGACAGTAGATGGTTATC
22	**lytB CBM up** / 5' lytB CBR8	+	**CCAGAGGGTGCAATGGCT**AGTCAGTGGATTAATCAAGCTTATG
23	**5' lytB CBR8** / lytB CBM up	-	**CATAAGCTTGATTAATCCACTGACT**AGCCATTGCACCCTCTGG
24	*NdeI* - **upstream region lytB**	+	GAAGGAGATATA*CATATG***GCAGCTGTTTCTCATGG**
25	*NdeI* - **5' lytB CBM**	+	GGAATTC*CATATG***AGTGATGGTACTTGGCAAGG**

Table S5. Primers (Cont.)

#	Primer Name	+/-	Sequence 5'->3'
26	*NdeI* - **5' lytB CBR1**	+	GAAGGAGATATA*CATATG***AGTGATGGTACTTGGCAAGG**
27	*NdeI* - **5' lytB CBR8**	+	GGAATTC*CATATG***AGTCAGTGGATTAATCAAGCTTATGTGAATGCTA**
28	*NdeI* - **5' lytB cat**	+	GGAATTC*CATATG***AATGCTGCTTACTATCAAGTAGTGCC**
29	*NdeI* - **5' GFP**	+	GAAGGAGATATA*CATATG***ATGATTTCTAAAGGTGAAGAATTG**
30	*PstI* - **3' lytB CBM**	-	TATTGCAC*TGCAG***TTTATTTGTAGCTTTTCCTCCAAGCC**
31	*PstI* - **3' lytB CBR8**	-	CAAGTTTTC*CTGCAG***CTGTACTTTGGCACCACTAGC**
32	*PstI* - **3' lytB cat**	-	CAAGTTTTC*CTGCAG***ATCTTTGCCACCTAGCTTC**
33	*PstI* - **3' lytB CBR4**	-	CAAGTTTTC*CTGCAG***TCTTTTCATCTTTCCATCTTGG**
34	*PstI* - **downstream region lytB**	-	CAAGTTTTC*CTGCA***GCCAACCTATCATGATTGCGC**
35	**Linker GFP** / 3'-GFP	-	**TCCGGATCCCTCGAG**TTTATACAATTCATCCATACCATGTG
36	**Linker GFP** / 5'-lytB	+	**CTCGAGGGATCCGGA**AGTGATGGTACTTGGC
37	**Linker GFP** / 5' lytB cat	+	**CTCGAGGGATCCGGA**AATGCTGCTTACTATCAAGTAG
38	**Linker GFP** / 5' lytB CBR8	+	**CTCGAGGGATCCGGA**AGTCAGTGGATTAATCAAGCTTATG
39	downstream region lytR	-	CCTGTCATCAACTTGGGTAG
40	upstream region lytR	+	AGGCAAAGGGTTTGCGTG
41	**[kan-rpsL]** / lytR-up	-	**CATTATCCATTAAAAATCAAACGG**ATTTCTACTAACCTATCAGTTTACCC
42	**[kan-rpsL]** / lytR-down	+	**GGAAAGGGGCCCAGGTCTCT**CTTTTGATACAAATAAAAAAATCAATCGTAGG
43	**LytR-up** / lytR-down	-	**CCTACGATTGATTTTTTTATTTGTATCAAAAG**ATTTCTACTAACCTATCAGTTTACCC
44	lytR -down	+	CTTTTGATACAAATAAAAAAATCAATCGTAGG
45	downstream region tacL	-	CTGTATAAACATAGCCATAAGC
46	upstream region tacL	+	ACCATGATTACTATGTTTATG
47	**[kan-rpsL]** / tacL-down	+	**GGAAAGGGGCCCAGGTCTCT**GTTTTATAAGTTTGAAATCTTC
48	**[kan-rpsL]** / tacL-up	-	**CATTATCCATTAAAAATCAAACGG**AATGAATCCTTTCTCTCCAA
49	**tacL-down** / tacL-up	-	**GAAGATTTCAAACTTATAAAAC**AATGAATCCTTTCTCTCCAAATC
50	**tacL-down**	+	GTTTTATAAGTTTGAAATCTTC